Ore Geology Reviews 141 (2022) 104670

Contents lists available at ScienceDirect

Ore Geology Reviews

journal homepage: www.elsevier.com/locate/oregeorev

Uplift-exhumation and preservation of the Yumugou Mo-W deposit, East Qinling, China: Insights from multiple apatite low-temperature thermochronology

Fan Yang [a,b,c,*], Gilby Jepson [d], Chao Liu [e], Zesheng Qian [a], Xuhuang Zhang [f], Yong Zhang [b], Stijn Glorie [c]

[a] Key Laboratory of Mineral Resources in Western China (Gansu Province), School of Earth Sciences, Lanzhou University, Lanzhou 730000, China
[b] MNR Key Laboratory of Metallogeny and Mineral Assessment, Institute of Mineral Resources, Chinese Academy of Geological Sciences, Beijing 100037, China
[c] Department of Earth Sciences, School of Physical Sciences, The University of Adelaide, South Australia 5005, Australia
[d] Department of Geosciences, University of Arizona, Tucson, AZ 85721, USA
[e] Shandong Provincial Lunan Geo-engineering Exploration Institute (The Second Geological Brigade of Shandong Geological Exploration Bureau), Jining 272100, China
[f] Luanchuan Bureau of Natural Resources, Luoyang 417500, China

ARTICLE INFO

Keywords:
Apatite thermochronology
Thermal history modeling
Exhumation and preservation
Porphyry-skarn Mo-W deposit
East Qinling Orogen

ABSTRACT

As a result of the continued depletion of shallow ore resources, there has been renewed focus on the tectonic preservation of mineralized systems. Specifically, it is vital to constrain the post-mineralization exhumation and preservation history of existing economic deposits, in order to identify new regions suitable for mineral exploration. In this study, we present results from apatite U-Pb, fission-track and (U-Th-Sm)/He thermochronological and associated thermal history modeling studies on the Yumugou Mo-W deposit within the world-class East Qinling Mo polymetallic metallogenic belt, central China. Our major aim is to constrain the exhumation history and to evaluate preservation potential of the Yumugou Mo-W deposit, and provide related guidance for mineral exploration in the East Qinling Orogen. Apatite U-Pb dating yield Early Cretaceous lower intercept Terra-Wasserburg ages in the range of 153–141 Ma, interpreted as crystallization age of apatite, coeval with the formation of Yumugou deposit (ca. 145 Ma). Integrated apatite fission-track and apatite (U-Th-Sm)/He dating give ages varying from Late Cretaceous to Early Paleogene, representing the post-mineralization cooling ages. We also integrate these age data with confined fission-track length measurements and geological constraints from previous studies into the thermal history models, the resulting models suggest three cooling pulses: 1) a phase of Early Cretaceous (125–100 Ma) rapid cooling, followed by 2) a phase of Late Cretaceous (100–73 Ma) slow cooling, before finally, 3) a phase of Late Cretaceous to Paleogene (73–50 Ma) rapid cooling. The Early Cretaceous rapid cooling pulse correlates temporally with extension tectonic setting in the East Qinling Orogen, the magma emplacement and post-magmatic rapid cooling at ca. 160–130 Ma in the Luanchuan region might cause related exhumation at ca. 125–100 Ma to upper crustal temperatures. The Late Cretaceous slow cooling possibly corresponds to regionally slow extensive erosion in response to crustal shortening triggered by the westward subduction of the Paleo-Pacific Plate at this time. The Late Cretaceous-Paleogene rapid cooling likely result from the major far-field effects of the Pacific Plate subduction and the sinistral strike-slip motion of the Tan-Lu Fault Zone, as well as possible minor expansion effects derived by the Paleogene India-Eurasia collision. Moreover, we adopt thermal history modeling method to determine cooling rate, exhumation rate and depth of different cooling stages. In comparison with the calculated exhumation depth (~5.6 km) and previously reported metallogenic depth (3–7 km) in the Luanchuan ore cluster, we infer that more than one kilometer metallogenic depth is theoretically preserved in the Yumugou Mo-W deposit. Combined the similar metallogenic setting and features with other giant Mo deposits in the East Qinling Orogen, we further suggest that the Mo deposits in this orogen possibly have underwent a similar degree of exhumation and show good prospecting potential.

* Corresponding author at: School of Earth Sciences, Lanzhou University, No.222 South Tianshui Road, Chengguan District, Lanzhou 730000, China.
E-mail address: fanyang@lzu.edu.cn (F. Yang).

https://doi.org/10.1016/j.oregeorev.2021.104670
Received 29 September 2021; Received in revised form 7 December 2021; Accepted 20 December 2021
Available online 28 December 2021

1. Introduction

Post-mineralization preservation history of ore deposit is a fundamental process to understand the tectonic evolution of ore deposit and would be helpful to guide mineral exploration (Márton et al., 2010; Sun et al., 2021; Gong et al., 2021). However, many studies only focus on ore genesis (Li et al., 2013; Wang et al., 2018), overlooking the final stage of the evolution of ore deposit. The exhumation and preservation of deposits are closely correlated with a regional uplift and exhumation history (Wang et al., 2008). Thus, reconstructing uplift and exhumation history has been a significant way to evaluate the preservation potential of ore deposit (Yuan, 2016). Porphyry Mo deposits are the important source of global metallic molybdenum (Mao et al., 2003; Klemm et al., 2008; Chen and Wang, 2011; Wu et al., 2017). Thus, understanding the mechanisms behind the exhumation and preservation of Mo deposits is important in the evaluation and exploration of future Mo resources (Zhao et al., 2016; Zhang et al., 2021a; Zhang et al., 2021b). China hosts the largest Mo reserves accounting for about 54% of global supply (Cao and Shen, 2018), most of them are classified as porphyry and are widely distributed throughout Qinling-Dabie and northeast China (Mao et al., 2009; Chen et al., 2012). However, limited characterization of the uplift and exhumation history of these deposits (Chen et al., 2015) has seriously hindered the understanding to their preservation history. With the increasing depletion of shallow Mo resources in recent decades (Li and Pirajno, 2017; Yang et al., 2017b; Xue et al., 2018), it is necessary to constrain the exhumation and preservation history of these deposits, which in turn is helpful for further exploration and prediction of prospecting targets.

Apatite [$Ca_5(PO_4)_3(F,OH,Cl)$], as one of common accessory minerals, is abundant in most igneous, metamorphic and sedimentary rocks, which is often utilized for dating via geo-, petro- and thermochronology (Zeitler et al., 1987; Chew et al., 2011, Yang et al., 2020a), such as Lu-Hf, U-Pb, fission-track and (U-Th-Sm)/He with closure temperature varying from 750 to 40 °C depending on the radiogenic system applied (Cherniak et al., 1991; Ketcham et al., 1999; Farley, 2000; Larsson and Söderlund, 2005). In general, the apatite Lu-Hf (750–675 °C) and U-Pb (500–425 °C) dating are used to reveal thermal and tectonic history of the deeper crust and date zircon-free magmatic rocks (Blackburn et al. 2011; Chew and Spikings, 2015). The apatite fission-track (120–60 °C) and (U-Th-Sm)/He (80–40 °C) thermochronological systems are popular for studying upper crustal and near-surface process (Braun et al. 2006). At present, apatite thermochronology has been widely used to quantify the timing of exhumation during compression and extension along active tectonic margins (Thiede et al., 2013), to determine vertical fault displacement (McInnes et al., 1999; Chew and Spikings, 2015), to reveal the thermal histories of sedimentary basins (Coutand et al., 2006) and deposits (Leng et al., 2018), and to constrain the timing of mineralization-related events (Huang et al., 2019). Through integrating the apatite fission-track and (U-Th-Sm)/He dating with associated thermal history modeling to constrain cooling history through apatite partial annealing zone (APAZ: 120–60 °C) (Laslett et al., 1982; Donelick and Miller, 1991) and partial retention zone (PRZ: 80–40 °C) (Stockli et al., 2000; Wolf et al., 1998), it would be very helpful to reveal upper crustal cooling signals from ~5 to 2 km and the final exhumation history of ore deposit (Yuan, 2016; Gong et al., 2021). With the rapid development of accurate high-precision dating methods, in-situ apatite U-Pb and fission-track double dating on same grain have been successfully used in several cases (Glorie et al., 2017; Yang et al., 2020a). When coupled with the apatite (U-Th-Sm)/He dating for triple-dating and thermal history modeling on same rocks, it is not only possible to rebuild continuous cooling paths (500–40 °C), but also accurately reveal the whole uplift and exhumation history from deeper crust to near-surface process (Carrapa et al., 2009; Jepson et al., 2018).

The East Qinling Orogen, one of significant Mo polymetallic metallogenic belts in China, hosts multiple world-class Mo ore clusters (e.g., Luanchuan, Jinduicheng) (Chen et al., 2009, Mao et al., 2008; Zhu et al., 2010; Li and Pirajno, 2017). The Luanchuan region with Mo reserves more than 2 million tons (Mao et al., 2008, 2011) makes up the most representative Mo ore cluster in the East Qinling Orogen, and includes several porphyry-skarn Mo deposits (e.g., Nannihu, Sandaozhuang) (Bao et al., 2014; Cao et al., 2015; Chen and Santosh, 2014; Yang et al., 2019). However, previous studies mostly involved geology, source of metallogenic fluid and material, metallochronology, and metallogenic dynamic setting (Mao et al., 2011; Li et al., 2012a; Zhang et al., 2015; Cao et al., 2015; Xue et al., 2018; Guo et al., 2018; Yang et al., 2019), the post-mineralization exhumation history and preservation potential of these Mo deposits are still unclear. The Yumugou porphyry-skarn Mo-W deposit, as a newly discovered and representative medium Mo deposit in the Luanchuan ore cluster, hosts in granite, skarn and hornstone at the inner and outer contact zone of the Huangbeiling granitic intrusion which has closely genetic links with the Mo-W mineralization. Yang et al. (2020a) proposed that the Huangbeiling pluton and neighboring granitic outcrops might have high potential for future W-Mo/Mo-W exploration in the Luanchuan ore cluster based on apatite chemical investigation. In addition, previous study focused largely on preliminary chacterization and prospecting work (TSGEI, 2009), the ore genesis and associated studies of post-mineralization of this deposit still remains poorly understood. Through constraining the uplift-exhumation and preservation history of this deposit, it is possible to quantify the exhumation-related values (e.g., rate, depth) for further guiding mineral exploration in similar mineralization systems. In general, the felsic granitoids host abundant accessory mineral of apatite, which can be utilized for thermochronology (Chew and Spikings, 2015). The ore-forming temperatures of these Mo deposits within the Luanchuan ore cluster have been determined in the range of 550–115 °C (Yang et al., 2009, 2013, 2015; Xue et al., 2021b), and coupled with the closure temperatures of different (geo-) thermochronometer dating systems. Therefore, we conduct systematic apatite U-Pb (550–425 °C), fission-track (120–60 °C) and (U-Th-Sm)/He (80–40 °C) triple-dating and related thermal history modeling studies on the major ore-hosting granites in the Yumugou Mo-W deposit. Our major objective is to reveal uplift and exhumation history of this deposit. Through correlation with published studies in the Luanchuan ore district, we also attempt to evaluate preservation potential of this deposit, and to provide related insights for future mineral exploration within the East Qinling Mo polymetallic metallogenic belt.

2. Geological setting

2.1. Regional geology

The Qinling Orogen located into the central section of the Central China Orogen and distributed between the North China and Yangtze Cratons (Fig. 1a) (Dong and Santosh, 2016; Wang et al., 2021a), and extends about 1000 km from west to east (Fig. 1b). The East Qinling Orogen in the eastern segment of this orogen is bordered to the south by the Longmenshan fault and to the north by the Sanbao fault, and consists of the northern margin of Yangtze Craton, South Qinling, North Qinling, Huaxiong block, and the southern margin of North China Craton, which are successively separated by the Mianlue, Shangdan and Luanchuan faults from south to north (Fig. 1b) (Bao et al., 2014; Dong et al., 2021). The East Qinling Orogen is also a concentrated Mo metallogenic belt in China (Chen and Santosh, 2014; Wang et al., 2017; Tang et al., 2021a, b; Li et al., 2021), and hosts numerous Mo-W-Pb-Zn-Ag polymetallic deposits (Li and Pirajno, 2017; Wang et al., 2021b; Zhang et al., 2021a; Zhang et al., 2021b) (Fig. 1c), with the Mo reserves more than 6 million tons (Li et al., 2012a; Gao et al., 2013), which includes multiple giant deposits with the reserve more than 0.5 million tons (e.g., Donggou, Nannihu, Shangfanggou, Yuchiling) as well as tens of Mo deposits (Mo reserve < 0.5 million tons) (e.g., Lengmengou, Shibaogou, Yuku) (Fig. 1c) (Yang et al., 2015; Zhou et al., 2020; Liu et al., 2021). As a result, the East Qinling Orogen forms one of the most significant Mo

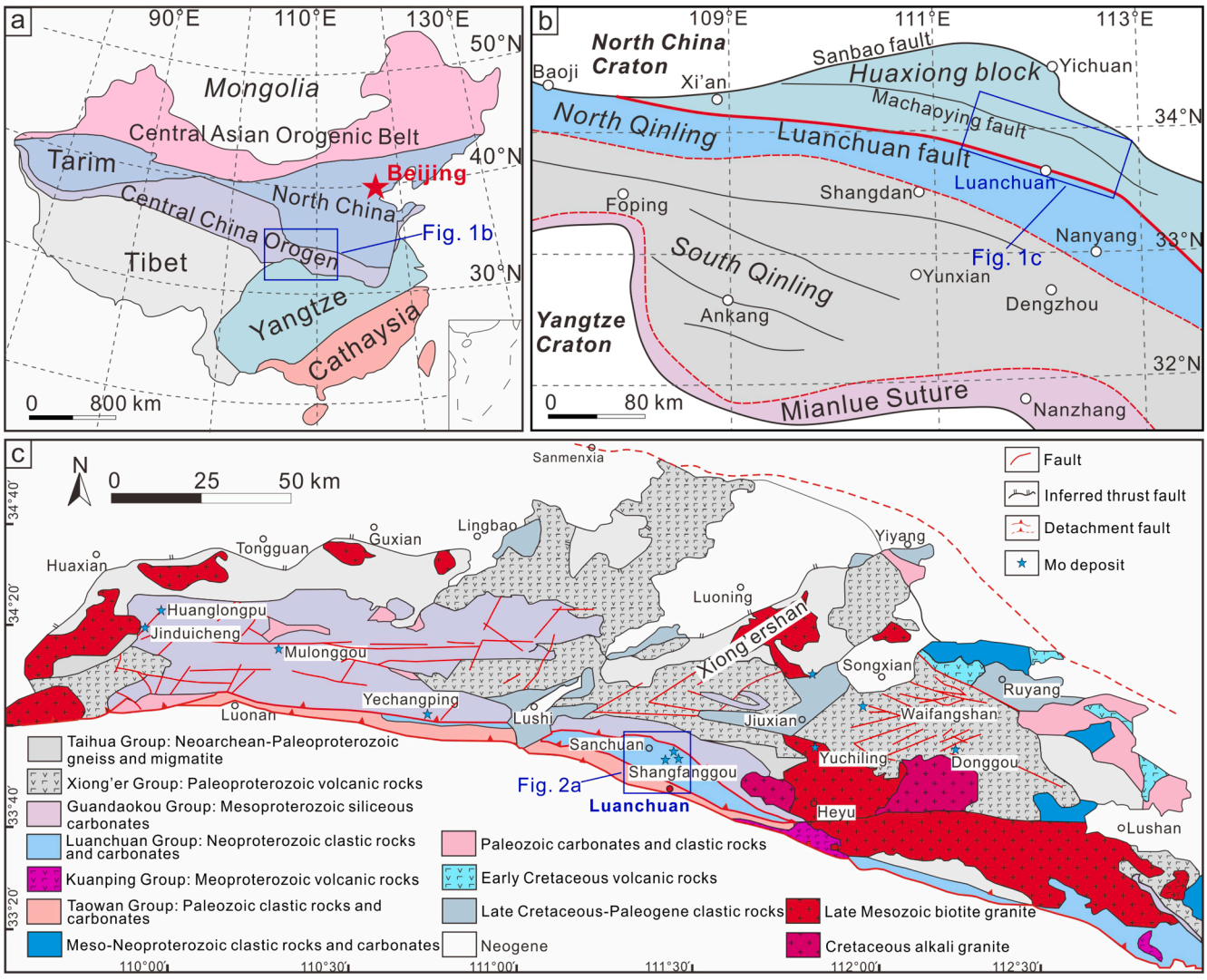

Fig. 1. (a) Tectonic division of China with the location of the East Qinling Orogen; (b-c) Tectonic subdivision and known Mo deposits of the East Qinling Orogen showing the location of the Luanchuan ore district (modified after Mao et al., 2011).

metallogenic belt in the world (Chen et al., 2009, Mao et al., 2008). Moreover, the East Qinling Orogen also recorded the tectonic evolution of the opening and closure of Paleo-oceans during the Late Paleozoic as well as the Triassic collision/subduction between the North China and Yangtze Cratons (Meng and Zhang, 2000; Yang et al., 2019). The known Mo deposits are largely concentrated in its northeastern terranes of Huaxiong and North Qinling within the East Qinling Orogen (Li et al., 2012a).

The Luanchuan Mo polymetallic ore district is situated in the northeastern East Qinling Orogen (Fig. 1b), and is one of the most representative Mo polymetallic clusters in this orogen (Fig. 2a) (Yang et al., 2017a, b; Li et al., 2018). Mo reserves are documented as more than 2 million tons, and account for ~40% of the whole East Qinling Mo metallogenic belt (Mao et al., 2008, 2011). The exposed strata of this ore district mainly include Kuanping, Taowan, Luanchuan and Guandaokou Groups from bottom to top (Fig. 2a), and consist mainly of Proterozoic and Paleozoic rocks, with unconformable contact relationships among these groups in sequence (Yang et al., 2017a; Wang et al., 2019a; Wang et al., 2019b; Xue et al., 2021a). The widely developed structures in this ore district are represented by the major NW-trending Luanchuan fault and its numerous branches as well as a few NE-trending secondary faults (Cao et al., 2015). Several WNW-striking thrust faults, subordinate NE-striking strike-slip faults and WNW-trending interlayer fractures are also developed in this ore district, and form the major ore-controlling structures related to regional Mo-W-Pb-Zn-Ag mineralization (Fig. 2a) (Li et al., 2015; Yang et al., 2020a). The intrusions in this ore district include Mesoproterozoic alkaline granite, Neoproterozoic metagabbro dykes and syenite porphyry, and the major Jurassic-Cretaceous granite (Fig. 2a). The Jurassic-Cretaceous granite show geochemical affinities of I-type granite correlated with extensional setting, and have close genetic links to known Mo polymetallic mineralization in the Luanchuan ore district (Zhang et al., 2015, 2018; Xue et al., 2018; Yang et al., 2019). Two significant ore fields with a similar metallogenic system are outlined into Nannihu and Yuku ore fields in the Luanchuan region (Fig. 2a), which host the porphyry-skarn type Mo-W deposits, the skarn type Zn deposits, and the hydrothermal-vein type Pb-Zn-Ag deposits from the center of porphyry to its periphery (Fig. 2a). The Nannihu ore field comprises the proximal porphyry-skarn type Mo-W deposits of Nannihu, Sandaozhuang and Shangfanggou deposits, the intermediate skarn type Zn deposits of Luotuoshan and Yinhegou deposits, and the distal hydrothermal-vein type Pb-Zn-Ag deposits of Lengshuibeigou, Sandaogou and Hongdonggou deposits (Cao et al., 2015) (Fig. 2a). The Yuku ore field includes the Dongyuku and Dawanggou deposits (porphyry-skarn type Mo-W deposits), the Zhongyuku deposit (skarn type Zn deposits), and the Bailugou, Xigou, Yindonggou and Laoangou deposits (hydrothermal-vein type Pb-Zn-Ag deposits) (Yang et al., 2017a)

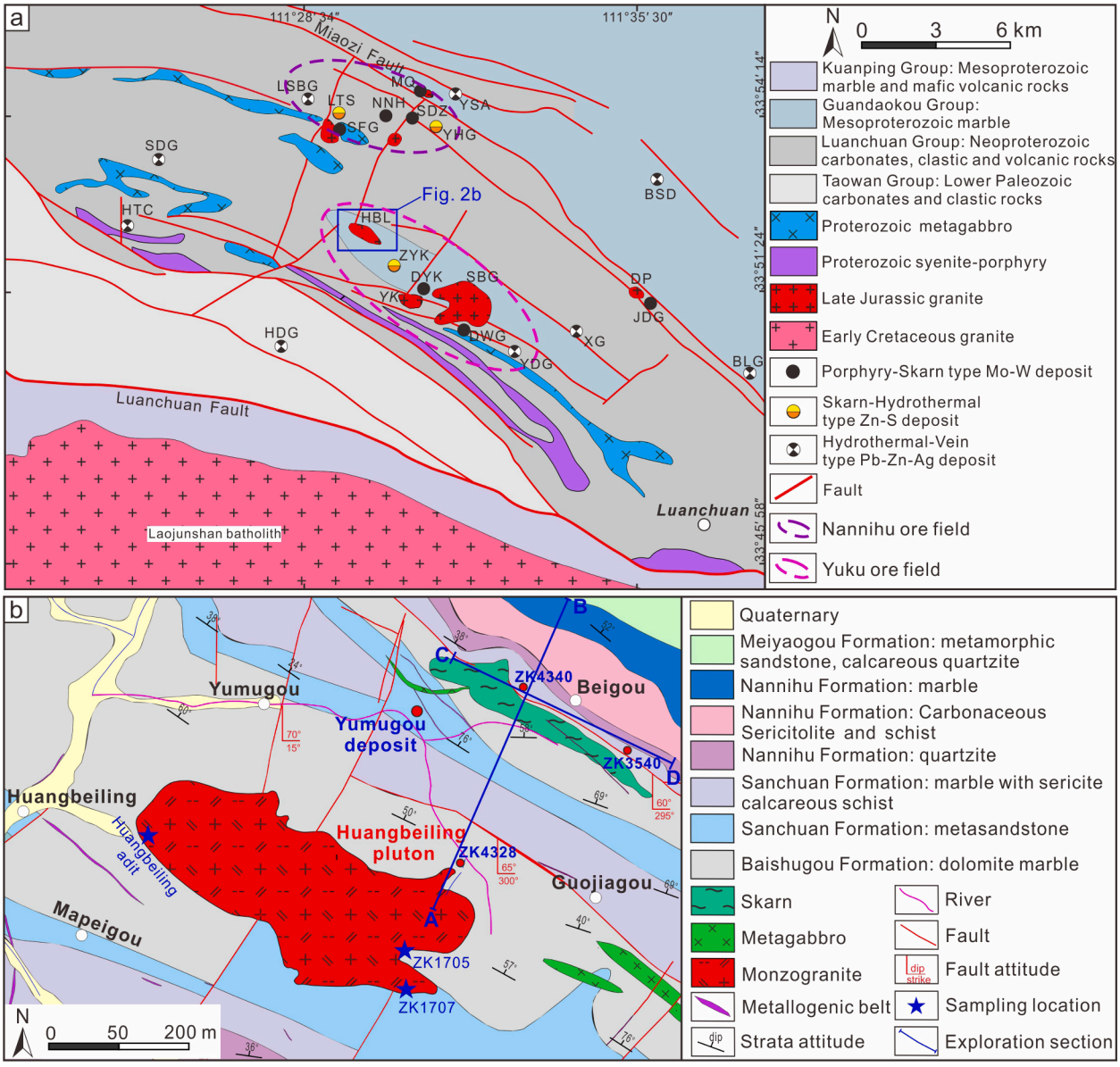

Fig. 2. (a) Geological map of the Luanchuan ore district (modified after Yang et al., 2019), (b) Geological map of the Yumugou Mo-W deposit (modified after TSGEI, 2009), showing the major intrusions, faults, strata, known ore deposits and orebodies and sampling locations. Deposit abbreviations: NNH, Nannihu; LTS, Luotuoshan; MQ, Maquan; SDZ, Sandaozhuang; SFG, Shangfanggou; YHG, Yinhegou; YSA, Yangshuao; SDG, Sandaogou; BSD, Baishadong; HTC, Hetaocha; BLG, Bailugou; LSBG, Lengshuibeigou; ZYK, Zhongyuku; DYK, Dongyuku; XG, Xigou; HDG, Hongdonggou; JDG, Jiudinggou; DWG, Dawanggou; YDG, Yindonggou. Intrusion abbreviations: HBL, Huangbeiling; YK, Yuku; DP, Daping, SBG, Shibaogou.

(Fig. 2a).

2.2. Deposit geology

The Yumugou Mo-W deposit, located in the central segment of Luanchuan ore district, is a newly discovered medium Mo deposit and forms one important part of the Yuku ore field (Fig. 2). The exposed strata contain Mesoproterozoic Baishugou Formation (Guandaokou Group) and Neoproterozoic Sanchuan, Nannihu, Meiyaogou and Dahongkou Formations (Luanchuan Group), which consist of metasandstone, dolomite marble, schist, slate and quartzite (TSGEI, 2009) (Fig. 2b). The major structures in this deposit comprise the main NW-trending faults with strike of 290-320° and dip in the range of 52-80° together with a few secondary NE-trending faults (strike: 10-40°, dip: 65-85°) (Fig. 2b) (TSGEI, 2009). The intrusive rocks include Proterozoic metagabbro and Late Jurassic to Early Cretaceous Huangbeiling porphyritic biotite monzogranite. The metagabbro is grayish to dark green colored and fine to medium grained, with a mineral assemblage of pyroxene, plagioclase and biotite, and intruded into the strata of Nannihu and Meiyaogou Formations as dikes along the NWW-trending faults in the north of this deposit, but no distinct genetic relationship with the Mo-W mineralization (TSGEI, 2009). The Huangbeiling monzogranite intrusion shows an irregular elliptical shape (Wu et al., 2015), with a length of about 4 km and a width of about 0.4 km, and is intruded into the strata of Baishugou and Sanchuan Formations (Fig. 2b). The outer margin of this pluton is characterized by relatively finer grained as well as less biotite and phenocrysts than those in the core of this pluton (TSGEI, 2009). These monzogranite rocks are pink to gray colored with porphyritic texture, and consist mainly of microcline, plagioclase and quartz phenocrysts together with fine grained felsic matrix with granitic texture, which have close genetic links with Mo-W mineralization (Zhao, 2018; Guo et al., 2018). The widely developed contact metasomatism

along the outer zone of the Huangbeiling intrusion results in calcium skarnization within the contact zone and nearby strata of Sanchuan Formation, and forms numerous skarns of garnet and garnet calcium ferrite (Fig. 3). The alteration of wall rocks mainly contains K-feldspathization, silicification, carbonate-zeolite and epidotization (TSGEI, 2009).

The Yumugou Mo-W deposit has inferred and predicted metal reserves of 60,590 tons Mo with an average grade of 0.06%, and 62,900 tons WO_3 with an average grade of 0.14% (TSGEI, 2009). Two orebodies are delineated in this deposit, with one major orebody distributed around the inner and outer contact zone of the Huangbeiling granitic intrusion as well as another minor orebody hosted into the strata of Sanchuan Formation in the south of this ore district (Fig. 3) (TSGEI, 2009). The major orebody shows an irregular ellipsoid shape and occurs as stratiform-like, with a length of 1300 m from east to west and a width of 640 m from north to south, covering an area of 0.85 square kilometers (TSGEI, 2009). The ore rocks are mainly hosted in the skarn, hornstone, metamorphic sandstone and granite porphyry together with a few in the metagabbro, marble and dolomite (TSGEI, 2009). The minor orebody also displays irregular stratiform-like occurrence, consistent with the occurrence of strata. The ore-hosting rocks consist mainly of skarn and hornstone, which were formed by the contact metasomatism with carbonatite of the Sanchuan Formation (TSGEI, 2009). The Mo ore rocks could be further divided into four types of felsic hornstone, diopside plagioclase hornstone, skarn and granite as well as some types of metagabbro, metasandstone and dolomite marble (Fig. 3). The ore mineral of these rocks mainly comprises disseminated and vein molybdenite, scheelite, sphalerite, galena and pyrite (TSGEI, 2009). The mineralization stages of this deposit are divided into these stages of skarn, K-feldspar quartz sulfide, quartz sulfide and zeolite carbonate sulfide, the dominant phase is the quartz sulfide stage represented by (quartz) veins of molybdenite and pyrite hosting in various ore-hosting rocks (TSGEI, 2009).

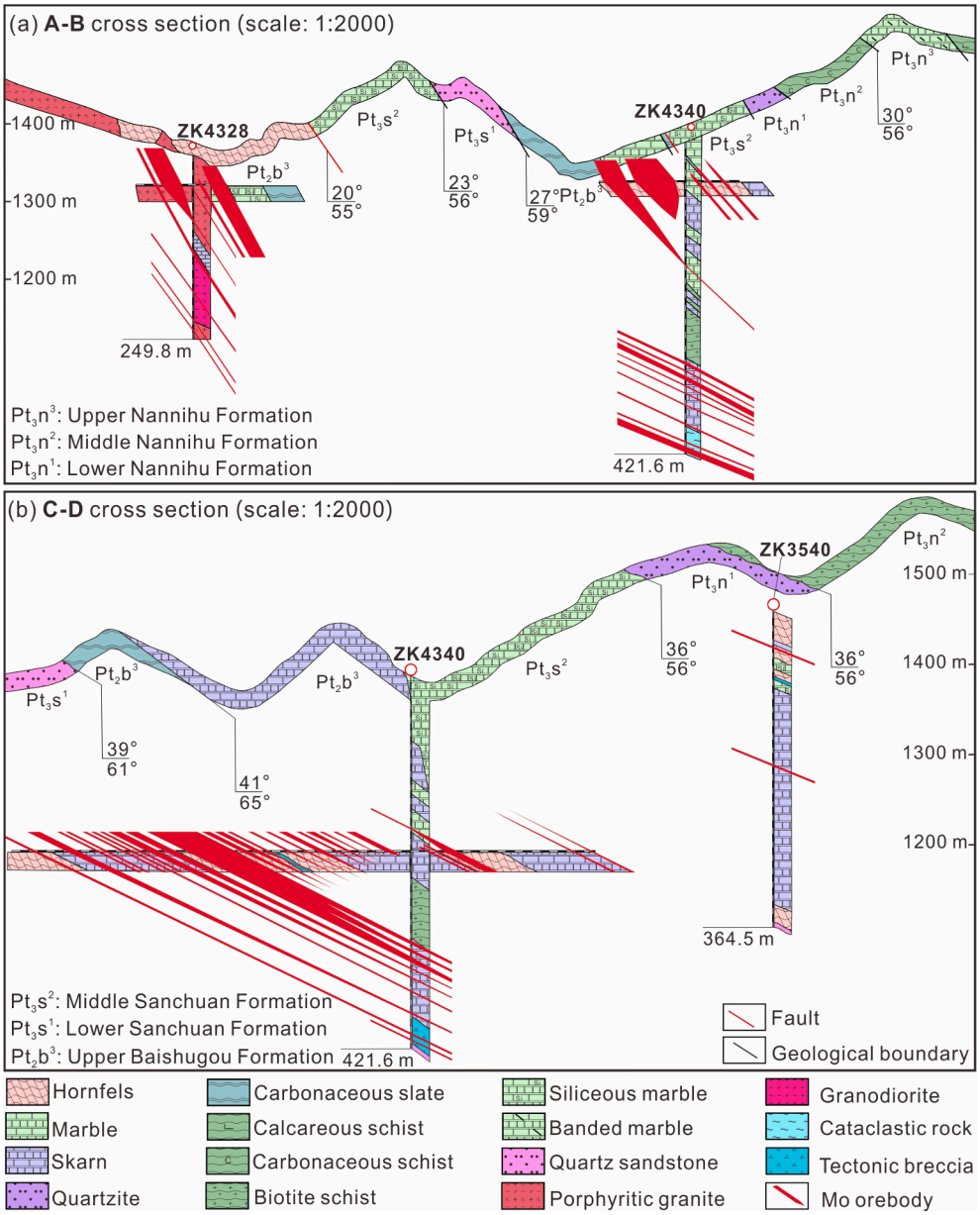

Fig. 3. Representative exploration cross sections of the Yumugou Mo-W deposit showing the spatial distribution of known Mo orebodies (modified after TSGEI, 2009).

3. Sampling and methods

3.1. Sampling and petrography

Representative samples collected from the surface exposures, adit quarry and boreholes of Huangbeiling intrusion in the Yumugou Mo-W deposit (Figs. 2, 4) were used for petrographic, in-situ apatite U-Pb and fission-track double dating, apatite (U-Th-Sm)/He dating, and associated thermal history modeling studies. Sample 17HBL-10–1 (N: 33°53′04.74″; E: 111°28′56.42″; H: 1446 m) was collected from a rock exposure at the top of Huangbeiling Mountain (Fig. 2b), and is off-white colored and fine grained monzogranite, with granitic texture and massive structure (Fig. 5a). Sample 19LC-3–10 was taken from borehole ZK1705 at a depth of ~357 m (Fig. 4), whereas sample 19LC-7–2 was sampled from borehole ZK1707 at a depth of ~248 m (Fig. 4). Both samples are pink colored monzogranites, and show granular texture with a mineral assemblage of K-feldspar, plagioclase, quartz and biotite (Fig. 5c, e). Sample 20HBL-1–5 monzogranite (N: 33°53′42.48″; E: 111°28′16.28″; H: 1117 m) is gray colored and medium grained, and consists mainly of felsic minerals and minor biotite, with several disseminated pyrites hosting in these minerals (Fig. 5g), which was taken from the adit quarry at the base of Huangbeiling Mountain (Fig. 2b).

Petrographic studies were performed on polished thin sections under one microscope at the School of Earth Sciences, Lanzhou University. Under thin sections (Fig. 5b, d, f, h), these studied samples all show typical granitic texture, and consist mainly of K-feldspar (30–45%), plagioclase (30–45%), quartz (20–30%) and biotite (1–5%). K-feldspar is medium grained (0.3–1.2 mm) and shows subhedral to anhedral granular texture and carlsbad twinning. Some K-feldspars intergrew with plagioclase, and host lots of biotite inclusions (Fig. 5d). Plagioclase is fine to medium grained (0.1–0.8 mm) and subhedral texture, characterized by polysynthetic twinning. Quartz is gray colored and mostly medium grained (0.4–1.5 mm), and displays subhedral to anhedral granular texture and wavy extinction. Biotite is yellow to brown colored with strong pleochroism and anhedral texture, and occurs as two forms

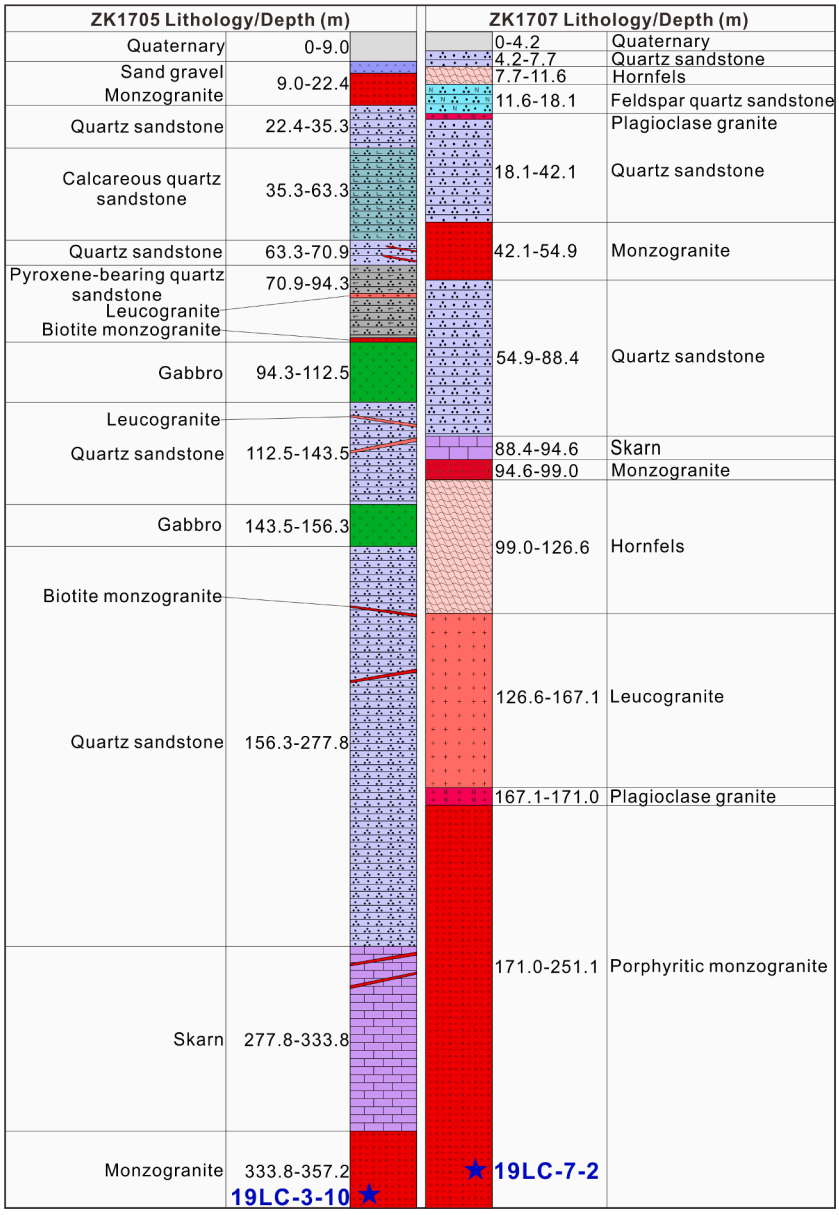

Fig. 4. Representative geological borehole sections of the Yumugou Mo-W deposit showing the major lithologic units and sampling locations (modified after TSGEI, 2009).

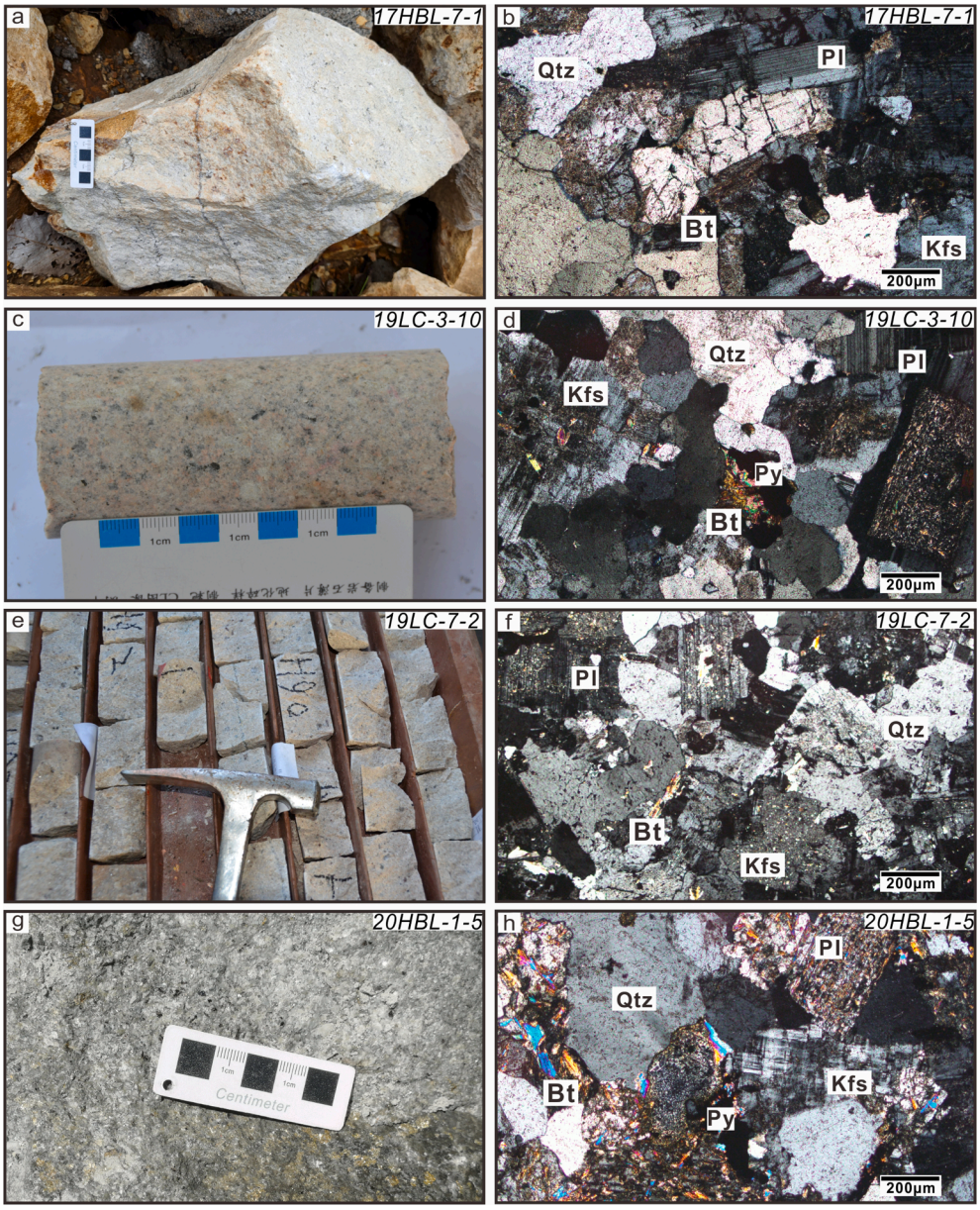

Fig. 5. Representative field photographs (a, c, e, g) and photomicrographs (b, d, f, h) of the studied Huangbeiling granitoids from the Yumugou Mo-W deposit. Mineral abbreviations: Pl, plagioclase; Kfs, K-feldspar; Qtz, quartz; Bt, biotite; Py, pyrite.

with one seen as inclusions in plagioclases and K-feldspars (Fig. 5d, h) and another one hosted in the gaps among felsic minerals (Fig. 5d, f). Pyrite as the major metallic mineral is fine grained, and displays anhedral texture and is hosted in gaps among felsic minerals (Fig. 5d, h).

3.2. Analytical methods

Apatite grains were separated through using standard mineral separation procedures at the Yu'neng Geological and Mineral Separation Survey Centre, Langfang, China, then picked and mounted in epoxy resin on a slide, finally via polishing to expose their interiors. The mounted apatite was etched by 5.5 mol/L HNO_3 solution at 20 ± 1 °C for 20 s to reveal their spontaneous fission tracks (Donelick et al. 2005). Fission track counting, track length and Dpar values were measured under an Olympus microscope at the University of Arizona, USA.

Apatite U-Pb (AUPb) and fission-track (AFT) double dating analyses (samples 19LC-3–10, 19LC-7–2, 20HBL-1–5) were concurrently performed on same grains through using a Photon Machine Analyte G2 Excimer 193 nm laser ablation system connected to a Thermo Element2 single collector High Resolution ICP-MS at the Arizona LaserChron Center, University of Arizona, USA. Spot size of ablations were set as 30 μm with a 5 Hz laser repetition rate, the reference materials include Madagascar (474.2 ± 0.4 Ma; Thomson et al., 2012), Mt. McClure (523.98 ± 0.12 Ma; Schoene and Bowring, 2006) and Durango apatite (31.44 ± 0.18 Ma; McDowell et al., 2005), the detailed analytical procedure is documented in Jepson et al. (2021). The AFT dating of sample 17HBL-10–1 was conducted within the Adelaide Microscopy, University of Adelaide, Australia, following the analytical method noted by Glorie et al. (2017). Data reduction was performed through the Iolite software (Paton et al. 2011; Chew et al. 2014), IsoplotR software (Vermeesch, 2018) was used to generate AUPb Tera-Wasserburg plots and ages, and RadialPlotter software (Vermeesch, 2009) was selected for calculating AFT central ages.

Apatite (U-Th-Sm)/He (AHe) dating were conducted using dissolution and isotope dilution of sample aliquots by ICP-MS at the Arizona Radiogenic Helium Dating Laboratory (ARHDL), University of Arizona,

USA. Apatite grains were measured under a Leica MZ16 stereozoom microscopes, and then selected these grains characterized by euhedral texture, grain width above 60 μm and no inclusions and fractures to continue AHe dating analysis. Durango apatite (31.44 ± 0.18 Ma; McDowell et al., 2005) was used as an analytical standard, AHe ages were calculated based on the procedure noted by Gautheron et al. (2009), following the detailed analytical procedure described in the Reiners (2005) and Reiners and Nicolescu (2006).

Thermal history modeling was established by inputting the newly obtained AFT and AHe ages, confined fission track length data and some geological constraints into QTQt software (Gallagher, 2012) to explore possible cooling paths. Kinetic parameters of the annealing model (Ketcham et al., 2007), Dpar (Burtner et al., 1994), radiation damage accumulation and annealing model of the Flowers et al. (2009), initial temperature constraints (400 ± 50 °C) of AUPb age, and the present temperature of 10 ± 10 °C were jointly used to constrain thermal history. The maximum likelihood, maximum posterior, maximum mode and expected models were outputted from the QTQt software, but only the expected model was used for each sample, following the detailed modeling procedure outlined by Glorie et al. (2019).

4. Results

4.1. Apatite U-Pb dating

Apatite U-Pb dates were obtained from samples 19LC-3–10, 19LC-7–2 and 20HBL-1–5, the AUPb dating results are given in Supplementary Table 1.

Thirty apatite grains from sample 19LC-3–10 yielded a Tera-Wasserburg linear array, with the lower intercept age at 141.1 ± 16.1 Ma (MSWD = 1.6) and ^{207}Pb corrected weighted mean ^{206}Pb-^{238}U ages in the range of 149.9–136.0 Ma (Fig. 6a). Thirty apatite grains from sample 19LC-7–2 also show one Tera-Wasserburg linear array (Fig. 6b), and yielded a lower intercept age at 153.1 ± 10.2 Ma (MSWD = 0.7) and ^{207}Pb corrected weighted mean ^{206}Pb-^{238}U ages ranging from 158.9 to 147.8 Ma. Thirty apatite grains from sample 20HBL-1–5 yielded a Tera-Wasserburg linear array, and gave a lower intercept age at 142.3 ± 7.9 Ma (MSWD = 1.0) (Fig. 6c), with ^{207}Pb corrected weighted mean ^{206}Pb-^{238}U ages between 148.7 and 135.6 Ma.

4.2. Apatite fission track dating

Apatite fission track analysis was conducted on the samples 17HBL-10–1, 19LC-3–10, 19LC-7–2 and 20HBL-1–5, the obtained AFT dating results are presented in Supplementary Table 2.

Sample 17HBL-10–1 taken from surface exposures yielded the youngest AFT central age of 58.2 ± 2.2 Ma (Fig. 7a), with the P(χ2) value of 7%, Dpar ranging from 0.9 to 1.6 μm and mean track length (MTL) of 12.4 ± 1.6 μm (Fig. 7e). Sample 19LC-3–10 collected from borehole ZK1705 at a depth of ~357 m yielded the oldest AFT central age of 114.1 ± 4.6 Ma (Fig. 7b) and MTL of 13.5 ± 1.0 μm (Fig. 7f), with the P(χ2) value of 61% and Dpar in the range of 1.4–2.7 μm. Sample 19LC-7–2 taken from borehole ZK1707 at a depth of ~248 m yielded a moderate AFT central age of 87.9 ± 4.5 Ma and Dpar varying from 1.5 to 3.0 μm (Fig. 7c) without MTL, the results also show P(χ2) value of 0% lower than 5% and not pass the χ2 test. Sample 20HBL-1–5 sampled from Huangbeiling adit yielded a relatively older AFT central age of 104.0 ± 4.3 Ma, MTL of 13.5 ± 1.3 μm (Fig. 7g) and Dpar ranging of 1.7–3.2 μm, with the P(χ2) value of 55% (Fig. 7d).

4.3. Apatite (U-Th-Sm)/He dating

Apatite (U-Th-Sm)/He dating was performed on the samples 19LC-3–10 and 20HBL-1–5, the obtained AHe data are shown in Supplementary Table 3.

Three apatite grains from sample 19LC-3–10 yielded single grain

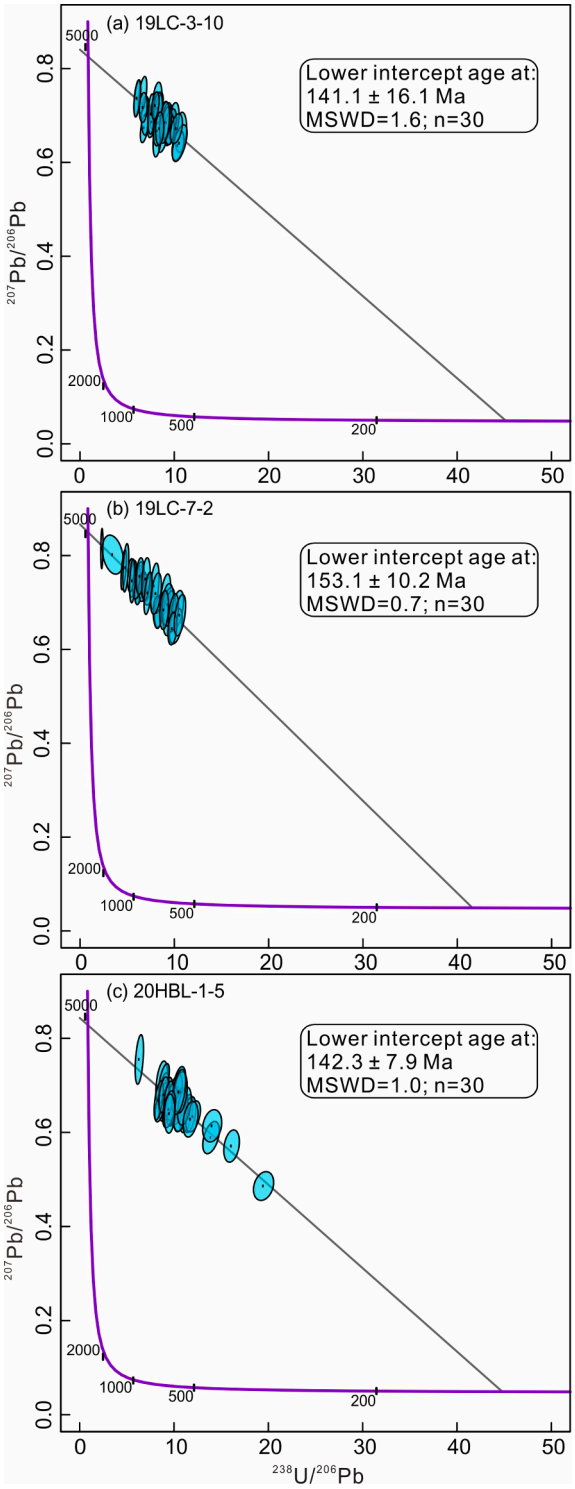

Fig. 6. Apatite U-Pb Terra-Wasserburg Concordia plots of the studied Huangbeiling granitoids from the Yumugou Mo-W deposit.

AHe ages in the range of 1296.1–93.5 Ma. Among these, two apatite grains show distinctly abnormal AHe ages of 1296.1 ± 15.3 and 228.0 ± 2.4 Ma with spherical equivalent radii (Rs) of 100.8–116.4 μm and effective uranium (eU) values varying from 29.4 to 30.5 ppm, which are much older than AUPb and AFT ages of the sample 19LC-3–10, likely resulting from lots of He-rich inclusions and fractures inside, and thus would be ruled out when modeling, and further interpretation of these AHe data also not be continued. One apatite yielded single grain AHe ages of 93.5 ± 1.0 Ma, Rs of 79.0 μm, and eU value of 40.1 ppm, and is

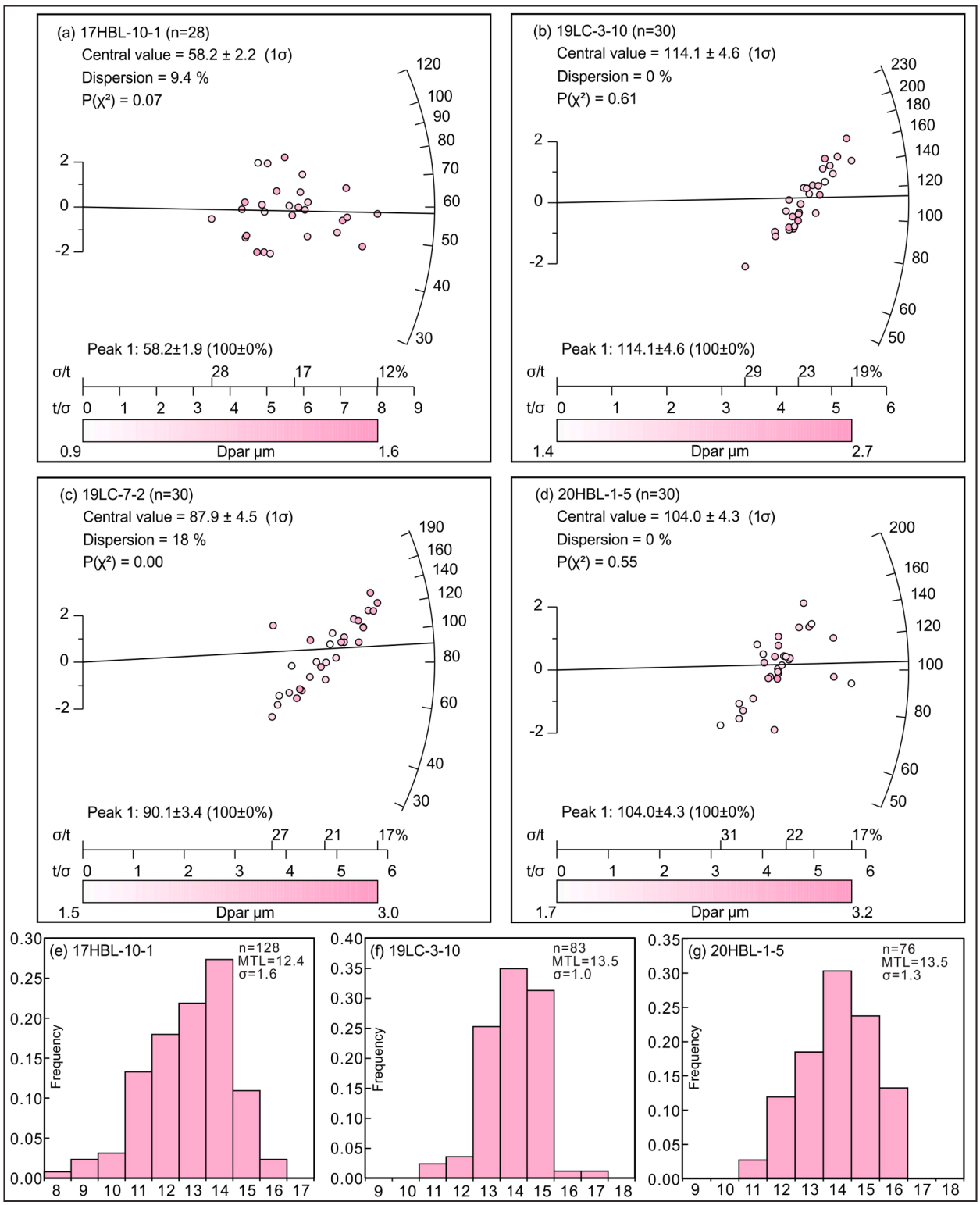

Fig. 7. Radial plots with Dpar values as color scale for apatite fission-track ages (a-d) and track length histograms (e-g) of the studied Huangbeiling granitoids from the Yumugou Mo-W deposit.

younger than corresponding AFT and AUPb ages, which could be used to model thermal history. Sample 20HBL-1–5 gave three single grain AHe ages of 81.8 ± 3.0, 77.1 ± 1.1 and 66.2 ± 0.8 Ma, respectively, with Rs of 66.4–99.7 μm and eU values of 26.3–33.4 ppm, which are mostly younger than corresponding AUPb and AFT ages of the sample 20HBL-1-5.

4.4. Thermal history modeling

Sample 17HBL-10–1 yielded 128 confined fission tracks (Fig. 7e), and the modeling results without AHe age data constraints show rapid cooling through the APAZ between 75 and 50 Ma (Fig. 8a, b). Thermal history model from sample 19LC-3–10 is constrained by 83 confined fission tracks (Fig. 7f) and AHe age data, the results display relatively

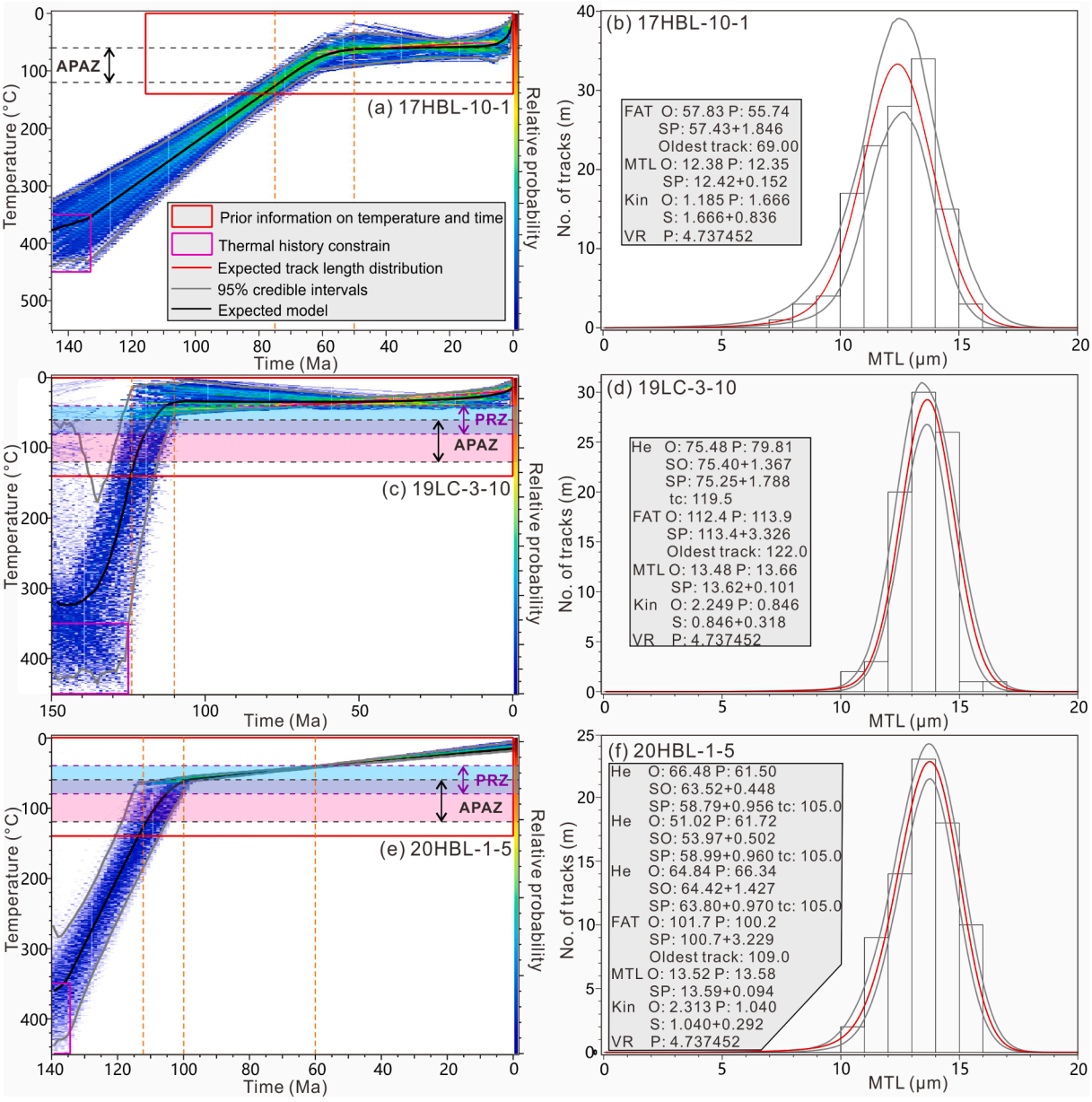

Fig. 8. Thermal history modeling results calculated by the QTQt software for expected thermal history probability density maps (a, c, e) and track length predictions (b, d, f) of the studied Huangbeiling granitoids from the Yumugou Mo-W deposit.

rapid cooling through the APAZ and PRZ at ca. 125–110 Ma (Fig. 8c, d). Sample 20HBL-1–5 gave 76 confined fission tracks (Fig. 7g), and the thermal history model with AHe age data constraints indicates two cooling stages, with one relatively rapid cooling stage through the APAZ at ca. 112–100 Ma and one slow cooling stage through the PRZ between 100 and 60 Ma (Fig. 8e, f). In addition, the measured MTL data are almost consistent with corresponding predicted data (Fig. 8b, d, f).

5. Discussion

5.1. Temporal evolution of the Yumugou deposit

Single-grain isochron corrected AUPb age data in this study show wide variation ranging between 166 and 112 Ma (Fig. 9b), with lower intercept ages in the range of 153.1–141.1 Ma (Fig. 6) and one age peak at ca. 143 Ma (Fig. 9b). These newly obtained AUPb ages are interpreted to represent the crystallization age of apatite, and are consistent with corresponding zircon U-Pb (ZUPb) ages of the Huangbeiling pluton (Qian et al., 2021) with ZUPb ages varying from 156.7 to 132.2 Ma and an age peak at ca. 143 Ma (Fig. 9a). Therefore, we interpret AUPb dates to reflect post-plutonic crystallization cooling (Kirkland et al. 2018). Previously published AUPb age data of other Late Mesozoic Luanchuan plutons also show wide variation in the range of 151.5–102.3 Ma with a major peak at ca. 141 Ma, and corresponding ZUPb ages vary from 176.3 to 108.0 Ma with a major peak at ca. 147 Ma (Yang et al., 2020a). Except for the Laojunshan batholith in the south of Luanchuan fault (Fig. 2a) which yielded Middle Cretaceous ZUPb and AUPb ages (Yang et al., 2019, Yang et al., 2020a, Yang et al., 2020b), the ZUPb and AUPb ages of other Luanchuan plutons overlap with the newly obtained AUPb ages of the Huangbeiling pluton within errors, further confirming rapid post-magmatic cooling below ~450 °C in response to shallow emplacement in the Luanchuan ore district (Yang et al., 2020a). Moreover, the ZUPb and AUPb ages of Huangbeiling pluton also record the first magmatic pulse (160–130 Ma) in the Luanchuan region, corresponding to the major regional magmatic pulses at ca. 160–125 Ma in the Qinling Orogen, which have been correlated with continuous northward

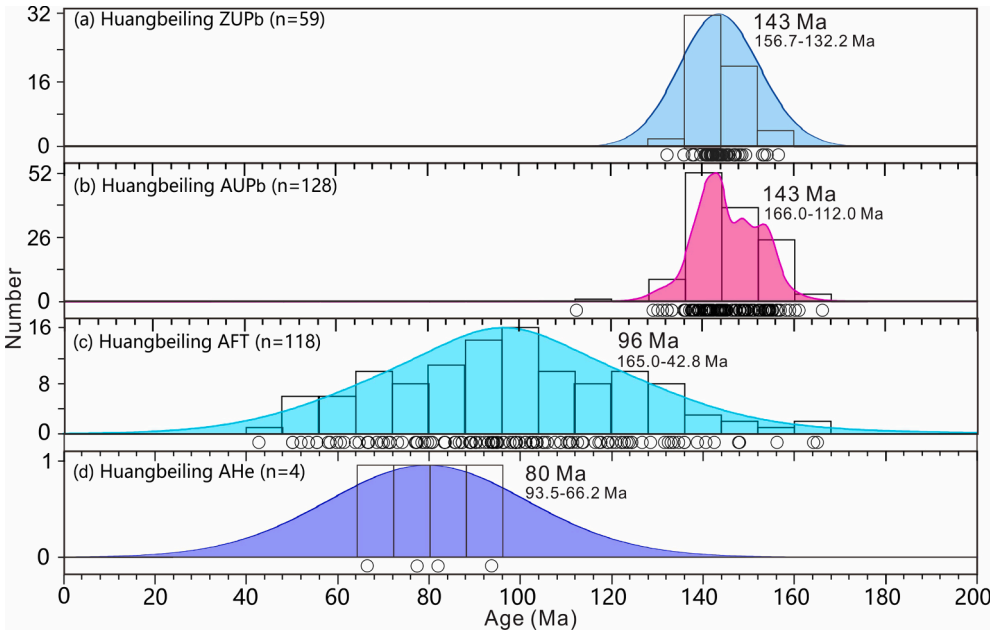

Fig. 9. Histograms of zircon U-Pb age (a), apatite U-Pb age (b), apatite fission-track age (c) and apatite (U-Th-Sm)/He age (d) of the studied Huangbeiling granitoids from the Yumugou Mo-W deposit. Zircon and apatite (sample HBL-10) U-Pb age data on the Huangbeiling granitic pluton are from Qian et al. (2021) and Yang et al. (2020a), respectively.

subduction of the Yangtze Craton beneath the North China Craton under a compression tectonic setting during pre-125 Ma (Li et al., 2018; Yang et al., 2019).

Previous studies have compiled metallogenetic ages (e.g., molybdenite Re-Os, sphalerite Rb-Sr, quartz Ar-Ar dating) of the Luanchuan hydrothermal-vein Pb-Zn-Ag and porphyry-skarn Mo-W deposits (Xue et al., 2018; Yang et al., 2019, 2020a), the results show ore-forming ages in the range of 147.5–135.7 Ma with a major peak at ca. 145 Ma (Yang et al., 2020a). Five molybdenite samples from the Yumugou porphyry-skarn Mo-W deposit yielded Re-Os model ages in a range of 146.7 ± 1.9 to 147.8 ± 2.4 Ma (unpublished), indicating that the Yumugou deposit also formed at ca. 145 Ma. Thus, we propose that the ZUPb and AUPb ages of the ore-hosting Huangbeiling pluton recorded coeval metallogenetic event, and have close temporal links with the Yumugou Mo-W mineralization during the Late Jurassic to Early Cretaceous. Further, we suggest that the AFT central ages of 114.1–58.2 Ma (Fig. 7) and associated AHe ages (93.5–66.2 Ma) (Fig. 9d) constrain the timing of post-mineralization cooling to the upper crust. All age data analyzed from this study shows age peak at ca. 96.0 Ma (Fig. 9c) for AFT and ca. 80.0 Ma for AHe ages (Fig. 9d), substantially younger than corresponding ZUPb and AUPb ages on the same samples of the Huangbeiling pluton. Specifically, the AUPb age peak (~143 Ma) is same with the ZUPb age peak (~143 Ma), the AFT age peak (~96 Ma) is ca. 50 Ma younger than the AUPb age peak (~143 Ma), whereas the AHe age peak (~80 Ma) is ca. 15 Ma younger than the AFT age peak (~96 Ma) (Fig. 9). Coupled with the closure temperatures of ZUPb (greater than 900 °C), AUPb (500–425 °C), AFT (120–60 °C) and AHe (80–40 °C) dating techniques, these age peaks suggest that the Yumugou Mo-W deposit underwent rapid host-rock thermal equilibration below ~450 °C after magma emplacement in the Late Jurassic to Early Cretaceous, with concomitant the formation of this deposit, followed by slow cooling below ~60 °C at ca. 143–96 Ma, and relatively rapid cooling below ~40 °C at ca. 96–80 Ma (Fig. 9).

5.2. Uplift-exhumation history of the Yumugou deposit

Thermal history models constructed in this study collectively suggest two stages of rapid cooling, with the first stage during the Early Cretaceous at ca. 125–100 Ma and the second stage in the Late Cretaceous to Paleogene (73–50 Ma) (Fig. 10a). These periods of rapid exhumation were interrupted by a period of slow cooling during the Late Cretaceous (100–73 Ma) in the PRZ (Fig. 10a). Moreover, thermal history model of the sample 17HBL-10–1 also shows a rapid cooling through the PRZ during the Neogene prior to cooling to the surface. However, as this model lacks AHe age data to precisely constrain, and thus the Neogene cooling event would not be further discussed in this study (Fig. 10a).

Early Cretaceous rapid cooling (125–100 Ma): Previous several studies proposed that the Luanchuan region was under compression during 160–130 Ma (Li et al., 2012a; Yang et al., 2019). The northward subduction of the Yangtze Craton beneath the North China Craton continued until ~125 Ma with concomitant crustal thickening and subducted slab break-off, rollback, or delamination (Li et al., 2018) and/or the southward intra-continental subduction of the North China Craton in response to *syn*-collisional tectonic setting during the Late Jurassic to Early Cretaceous (Dong et al., 2011, 2016; Yang et al., 2019; Qian et al., 2021). Following the tectonic setting was transformed from compression to extension at ca. 125 Ma (Xue et al., 2018; Yang et al., 2019). This extension tectonics is correlated with the N-S trending post-collisional extension between the North China and Yangtze Cratons and the E-W trending back-arc extension induced by the Paleo-Pacific Plate subduction from the east during the Early Cretaceous (Yang et al., 2019), resulting in asthenospheric upwelling, mafic magma underplating, and crustal melting (Li et al., 2018). Moreover, the Luanchuan granitoids underwent magma emplacement and post-magmatic rapid cooling at ca. 160–130 Ma revealed by previously published ZUPb and AUPb ages in response to shallow emplacement (Yang et al., 2019, 2020a), and rapid cooling to the shallow surface, which likely caused related exhumation at ca. 125–100 Ma. Thus, we interpret the Early Cretaceous rapid cooling as a response to tectonic extension derived by the westward subduction of the Paleo-Pacific Plate, accompanied by with asthenospheric upwelling and lithospheric thinning, which possibly result in the rapid cooling of the Late Jurassic to Early Cretaceous magmatism in the Luanchuan ore district.

Late Cretaceous slow cooling (100–73 Ma): During the Late Cretaceous to Early Paleogene, the Paleo-Pacific Plate (Izanagi/Kula)

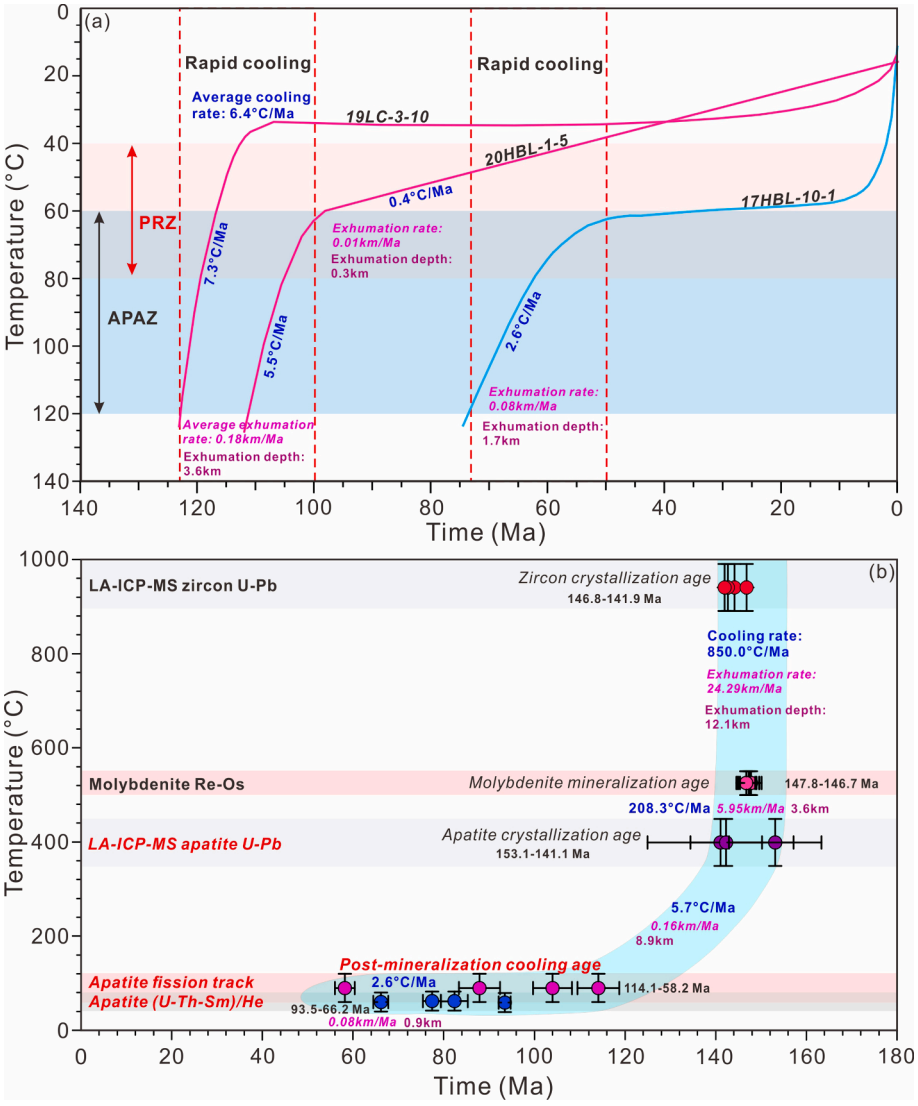

Fig. 10. (a) Thermal history modeling results integrated from this study; (b) Temperature-time path of multiple geochronometers from previous studies (Yang et al., 2020a; Qian et al., 2021) and this study in the Yumugou Mo-W deposit.

underwent a period of crustal deformation and basin evolution in East Asia (Cho et al., 2016). The Izanagi Plate underwent rapid N- or NW-directed oblique subduction beneath the Eurasian Plate at ca. 135–85 Ma or until ca. 60 Ma (Maruyama et al., 1997), Subsequently, the Kula Plate underwent west-northwestward orthogonal subduction at ca. 85–64 Ma (Engebretson et al., 1985). The Late Cretaceous slow cooling identified in this study corresponds temporally to the response with the tectonic evolution of the East Asia during the Late Cretaceous. Given the distal nature of the study area (about ~1000 km) from the margin of eastern Asia, we correlate the Late Cretaceous slow cooling pulse of the Luanchuan region with the far-field effect of the Paleo-Pacific Plate (Izanagi/Kula) (De Grave and Buslov, 2007). Furthermore, this period of slow cooling also corresponds to the timing of rifting and exhumation history of Bohai Bay and adjacent basins in the East Asia (Yang et al., 2020b).

Late Cretaceous to Paleogene rapid cooling (73–50 Ma): Previous studies suggested that the East Asia encountered lateral extrusion toward the east triggered by the far-field effect of the India-Eurasia collision during the Paleogene (Tapponnier and Molar, 1997; Grimmer et al., 2002), the initial India-Eurasia collision is also widely accepted to have started during the Paleogene (Patriat and Achache, 1984; Jin et al., 2018). In addition, the largest continental-scale NNE-striking fault zone of Tan-Lu Fault Zone (TLFZ) in the eastern China (Xu and Zhu, 1994), located in the northeast of the Luanchuan region, underwent continued sinistral strike-slip motion induced by the NNW-directed Pacific subduction during 65–55 Ma, and ended at ca. 55 Ma derived by the far-field effect of the NNE-directed India-Eurasia collision (Wang et al., 2019a; Wang et al., 2019b). The Pacific Plate was subsequently changed from NNW to WNW in the subduction direction, which modified the stress balance on the TLFZ, resulting in dextral motion of the TLFZ at ca. 48–42 Ma (Wang et al., 2019a; Wang et al., 2019b). The Pacific Plate was also orthogonally subducted west-northwestward at ca. 64–53 Ma, afterwards obliquely subducted northward beneath the eastern Asia at ca. 53–48 Ma (Engebretson et al., 1985). The ca. 73–50 Ma rapid cooling pulse revealed in the sample 17HBL-10–1 (Fig. 10a) is also constrained by its AFT central age of ~58.2 Ma and relatively short MTL value (Fig. 7e). Thus, we propose that the Late Cretaceous to Paleogene rapid cooling possibly response to the major far-field effects from the eastern Pacific Plate subduction and the northeastern sinistral strike-slip motion of TLFZ at ca. 65–55 Ma, as well as possible minor expansion effects of the Tibetan plateau induced by the Paleogene India-Eurasia collision from the southwest.

5.3. Preservation and exploration of the Yumugou deposit

Exhumation rate and depth of ore deposits are usually calculated through low-temperature thermochronological data, the frequently-used means mainly include age-closure, age-elevation, mineral-pair and thermal history modeling methods (Ding et al., 2007). Considering these constraints of short horizontal distance and large vertical distance of sampling demand for age-elevation method and uniformly uplift to the surface for age-closure method, and coupled with spatial location of sampling in this study and the muti-method apatite U-Pb, fission-track and (U-Th-Sm)/He triple-dating techniques on same rocks, we adopt the mineral-pair and thermal history modeling methods to calculate exhumation rate and depth in this study. A geothermal gradient of 35 °C/km (Li et al., 2011) and the closure temperatures of ZUPb (950 °C), molybdenite Re-Os (525 °C), AUPb (400 °C), AFT (90 °C) and AHe (60 °C) were adopted in this study. Additionally, the metallogenic depth of the Yumugou Mo-W deposit was roughly estimated through fluid inclusion data of Mo polymetallic deposits from previous studies in the Luanchuan ore district (Yang et al., 2009, 2013; Xue et al., 2021b), the equations related to exhumation were based on: 1) Cooling rate = $(T_2 - T_1)/(t_2 - t_1)$, 2) Exhumation rate = Cooling rate/geothermal gradient, and 3)Exhumation depth = Exhumation rate × $(t_2 - t_1)$ (noted that: T is the closure temperature, while t represents the age) (Ding et al., 2007; Li et al., 2019).

Exhumation rate and depth of the Yumuogu deposit were calculated via multiple geochronometers in this study (Fig. 10b) (McInnes et al., 2005), the results show a very rapid cooling rate of 850.0 °C/Ma, an exhumation rate of 24.29 km/Ma and an exhumation depth of 12.1 km during the closure temperature from ZUPb to molybdenite Re-Os (MoRO) dating systems, followed by a moderate cooling rate of 208.3 °C/Ma, an exhumation rate of 5.95 km/Ma and an exhumation depth of 3.6 km from MoRO to AUPb closure temperature. Given that the Yumugou M−Wo deposit was determined to form at ca. 145 Ma, these ages of ZUPb, MoRO and AUPb of the Huangbeiling pluton are almost equal within error, we thus argue that the Huangbeiling pluton has had at least 15 km depth denuded during pre-145 Ma. Subsequently, the Yumugou deposit underwent a slow cooling rate of 5.7 °C/Ma, an exhumation rate of 0.16 km/Ma and an exhumation depth of 8.9 km during the AUPb to AFT closure temperature, eventually with a relatively slower cooling rate of 2.6 °C/Ma, an exhumation rate of 0.08 km/Ma and an exhumation depth of 0.9 km from AFT to AHe closure temperature. Accordingly, we conclude that the Yumugou deposit following crystallization has had at least 9.8 km of material removed above it. However, previous fluid inclusion studies in the Luanchuan ore district have estimated the metallogenic depth of Mo deposits in the range of 3–7 km (Yang et al., 2009, 2013; Xue et al., 2021b). The calculated exhumation depth (~9.8 km) of the Yumugou Mo-W deposit does not correlate with the determined metallogenic depth (3–7 km) of the Luanchuan Mo deposits, but it possibly suggests that metallogenic depth was perhaps closer to 7 km, rather than to 3 km. Thus, we propose that this rough algorithm based on multiple geochronometers could not precisely evaluate the exhumation degree of study object, but it can be used as related constraints to accurately restrain the thermal history paths during modeling.

Thermal history models of the Yumugou deposit in this study (Figs. 8, 10a) were constrained by AFT and AHe ages, confined fission track length data and some other geological constraints, and thus these models are relatively reliable and can accurately reveal the exhumation history of this deposit. The modeling results suggest a rapid cooling rates in the range of 7.3–5.5 °C/Ma (mean value: 6.4 °C/Ma), an average exhumation rate of 0.18 km/Ma and an exhumation depth of 3.6 km in the first rapid cooling stage (125–100 Ma), followed by a slow cooling rate of 0.4 °C/Ma, an exhumation rate of 0.01 km/Ma and an exhumation depth of 0.3 km at ca. 100–73 Ma, and afterwards underwent another phase of rapid cooling (73–50 Ma) with a relatively fast cooling rate of 2.6 °C/Ma, an exhumation rate of 0.08 km/Ma and an exhumation depth of 1.7 km (Fig. 10a). Thus, we could conclude that the Yumugou deposit has been exhumed at least 5.6 km after ca. 145 Ma. In comparison with previously determined metallogenic depth (3–7 km), we theoretically deduce that there will be possible more than 1 km metallogenic depth preserved in the Yumugou Mo-W deposit. In addition, most of exploratory boreholes within the Yumugou Mo-W deposit show shallow prospecting depths at 200–500 m (Fig. 3), thus suggesting good potential for mineral exploration. By comparison with other giant Mo deposits in the East Qinling Mo polymetallic metallogenic belt (e.g., Jinduicheng, Yuchiling, Donggou) (Zhu et al., 2010; Mao et al., 2008, 2011; Li et al., 2012b; Yang et al., 2012, Yang et al., 2015), it can be seen that similar metallogenic setting and features of Mo deposits are hosted in this orogen. Thus, we further infer that these Mo deposits in the East Qinling Orogen likely have underwent a similar degree of exhumation after formation and show good potential for prospecting exploration.

6. Conclusions

(1) The Yumugou Mo-W deposit yielded AUPb ages in the range of 166–112 Ma, almost consistent with the formation of this deposit, and also gave AFT central ages varying from 114.1 to 58.2 Ma and AHe dates between 93.5 and 66.2 Ma, representing the post-mineralization cooling ages.
(2) Three cooling stages are revealed in this study, with the rapid cooling in the 125–100 Ma, slow cooling at ca. 100–73 Ma, and another rapid cooling in the 73–50 Ma, which are correlated with the tectonic evolution of the Paleo-Pacific and Pacific Plates subduction beneath the eastern Asia in the Meso-Cenozoic and the TLFZ motion during the Paleogene, as well as possible minor far-field effects from the Paleogene India-Eurasia collision.
(3) More than 1 km metallogenic depth is theoretically preserved in the Yumugou Mo-W deposit. When combined with similar metallogenic setting and features of other Mo deposits in the East Qinling Orogen, a similar exhumation degree of Mo deposits and good potential for mineral exploration are inferred in this orogen.

Declaration of Competing Interest

The authors declare that they have no known competing financial interests or personal relationships that could have appeared to influence the work reported in this paper.

Acknowledgments

We thank Prof. M. Santosh for his help at the University of Adelaide, Australia, Dr. Fei Xue for his help with regard to the sampling in the field, Dr. Uttam Chowdry for his assistance with helium analysis, and Prof. Juxing Tang for his support related to the application of opening foundation. The editors and two anonymous reviewers are also appreciated for their helpful suggestions and comments to improve the quality of this paper. This study was jointly supported by the Natural Science Foundation of Gansu Province (Grant No. 20JR10RA630), the Opening Foundation of MNR Key Laboratory of Metallogeny and Mineral Assessment (Grant No. ZS2106), the China Scholarship Council (File No. 201706400016), the “Innovation star” Project of Outstanding Post-graduate of Gansu Province (Grant No. 2021CXZX-105), the Fundamental Research Funds for the Central Universities (Grant No. LZUJBKY-2020-38), and the Guiding Special Funds of “Double First-Class (First-Class University & First-Class Disciplines)” (Grant No. 561119201) of Lanzhou University, China.

Appendix A. Supplementary data

Supplementary data to this article can be found online at https://doi.org/10.1016/j.oregeorev.2021.104670.

References

Bao, Z., Wang, C.Y., Zhao, T., Li, C., Gao, X., 2014. Petrogenesis of the Mesozoic granites and Mo mineralization of the Luanchuan ore field in the East Qinling Mo mineralization belt, Central China. Ore Geol. Rev. 57, 132–153.

Blackburn, T., Bowring, S.A., Schoene, B., Mahan, K., Dudas, F., 2011. U-Pb thermochronology: creating a temporal record of lithosphere thermal evolution. Contrib. Miner. Petrol. 162 (3), 479–500.

Braun, J., Van der Beek, P., Batt, G., 2006. Quantitative Thermochronology: Numerical Methods For The Interpretation Of Thermochronological Data. Cambridge University Press.

Burtner, R.L., Nigrini, A., Donelick, R.A., 1994. Thermochronology of Lower Cretaceous source rocks in the Idaho-Wyoming thrust belt. AAPG Bull. 78, 1613–1636.

Cao, C., Shen, P., 2018. Advances and problems in study of porphyry molybdenum deposits. Geol. Rev. 64, 477–497 (in Chinese with English abstract).

Cao, H.-W., Zhang, S.-T., Santosh, M., Zheng, L., Tang, L.i., Li, D., Zhang, X.-H., Zhang, Y.-H., 2015. The Luanchuan Mo-W-Pb-Zn-Ag magmatic-hydrothermal system in the East Qinling metallogenic belt, China: Constrains on metallogenesis from C-H-O-S-Pb isotope compositions and Rb-Sr isochron ages. J. Asian Earth Sci. 111, 751–780.

Carrapa, B., DeCelles, P.G., Reiners, P.W., Gehrels, G.E., Sudo, M., 2009. Apatite triple dating and white mica 40Ar/39Ar thermochronology of syntectonic detritus in the Central Andes: A multiphase tectonothermal history. Geology 37, 407–410.

Chen, H., Hu, J., Wu, G., Shi, W., Geng, Y., Qu, H., 2015. Apatite fission-track thermochronological constraints on the pattern of late Mesozoic-Cenozoic uplift and exhumation of the Qinling Orogen, central China. J. Asian Earth Sci. 114, 649–673.

Chen, Y.J., Santosh, M., 2014. Triassic tectonics and mineral systems in the Qinling Orogen, central China. Geol. J. 4, 338–358.

Chen, Y.J., Zhai, M.G., Jiang, S.Y., 2009. Significant achievements and open issues in study of orogenesis and metallogenesis surrounding the North China continent. Acta Petrol. Sinica 25, 2695–2726 (in Chinese with English abstract).

Chen, Y.J., Zhang, C., Li, N., Yang, Y.F., Deng, K., 2012. Geology of the Mo deposits in Northeast China. J. Jilin Univ. (Earth Science Edition) 42, 1223–1268 (in Chinese with English abstract).

Chen, Y., Wang, Y., 2011. Fluid inclusion study of the Tangjiaping Mo deposit, Dabie Shan, Henan Province: implications for the nature of the porphyry systems of post-collisional tectonic settings. Int. Geol. Rev. 53 (5-6), 635–655.

Cherniak, D.J., Lanford, W.A., Ryerson, F.J., 1991. Lead diffusion in apatite and zircon using ion implantation and Rutherford backscattering techniques. Geochim. Cosmochim. Acta 55 (6), 1663–1673.

Chew, D.M., Petrus, J.A., Kamber, B.S., 2014. U-Pb LA-ICPMS dating using accessory mineral standards with variable common Pb. Chem. Geol. 363, 185–199.

Chew, D.M., Spikings, R.A., 2015. Geochronology and thermochronology using apatite: time and temperature, lower crust to surface. Elements 11 (3), 189–194.

Chew, D.M., Sylvester, P.J., Tubrett, M.N., 2011. U-Pb and Th-Pb dating of apatite by LA-ICPMS. Chem. Geol. 280 (1-2), 200–216.

Cho, H., Son, M., Cheon, Y., Sohn, Y.K., Kim, J.-S., Kang, H.-C., 2016. Evolution of the Late Cretaceous Dadaepo Basin, SE Korea, in response to oblique subduction of the proto-Pacific (Izanagi/Kula) or Pacific plate. Gondwana Res. 39, 145–164.

Coutand, I., Carrapa, B., Deeken, A., Schmitt, A.K., Sobel, E.R., Strecker, M.R., 2006. Propagation of orographic barriers along an active range front: Insights from sandstone petrography and detrital apatite fission-track thermochronology in the intramontane Angastaco basin, NW Argentina. Basin Res. 18 (1), 1–26.

De Grave, J., Buslov, M.M., Van den haute, P., 2007. Distant effects of India-Eurasia convergence and Mesozoic intracontinental deformation in Central Asia: Constraints from apatite fission-track thermochronology. J. Asian Earth Sci. 29 (2-3), 188–204.

Ding, R.X., Zhou, Z.Y., Wang, W., 2007. Modeling exhumation rates of orogenic belts with low-temperature thermochronological data. Adv. Earth Sci. 22, 447–456.

Donelick, R.A., Miller, D.S., 1991. Enhanced TINT fission track densities in low spontaneous track density apatites using 252Cf-derived fission fragment tracks: A model and experimental observations. Internat. J. Radiat. Appl. Instrum. Part D Nucl. Tracks Radiat. Meas. 18 (3), 301–307.

Donelick, R.A., O'Sullivan, P.B., Ketcham, R.A., 2005. Apatite fission-track analysis. Rev. Mineral. Geochem. 58, 49–94.

Dong, Y., Sun, S., Santosh, M., Zhao, J., Sun, J., He, D., Shi, X., Hui, B.o., Cheng, C., Zhang, G., 2021. Central China Orogenic Belt and amalgamation of East Asian continents. Gondwana Res. 100, 131–194. https://doi.org/10.1016/j.gr.2021.03.006.

Dong, Y., Zhang, G., Neubauer, F., Liu, X., Genser, J., Hauzenberger, C., 2011. Tectonic evolution of the Qinling orogen, China: review and synthesis. J. Asian Earth Sci. 41 (3), 213–237.

Dong, Y., Santosh, M., 2016. Tectonic architecture and multiple orogeny of the Qinling Orogenic Belt, Central China. Gondwana Res. 29 (1), 1–40.

Dong, Y., Yang, Z., Liu, X., Sun, S., Li, W., Cheng, B., Zhang, F., Zhang, X., He, D., Zhang, G., 2016. Mesozoic intracontinental orogeny in the Qinling Mountains, central China. Gondwana Res. 30, 144–158.

Engebretson, D.C., Cox, A., Gordon, R.G., 1985. Relative motions between oceanic and continental plates in the Pacific basin. Geol. Soc. Am. Spec. Papers 206, 1–49.

Farley, K.A., 2000. Helium diffusion from apatite: General behavior as illustrated by Durango fluorapatite. J. Geophys. Res. Solid Earth 105, 2903–2914.

Flowers, R.M., Ketcham, R.A., Shuster, D.L., Farley, K.A., 2009. Apatite (U–Th)/He thermochronometry using a radiation damage accumulation and annealing model. Geochim. Cosmochim. Acta 73 (8), 2347–2365.

Gallagher, K., 2012. Transdimensional inverse thermal history modeling for quantitative thermochronology. Journal of Geophysical Research: Solid. Earth 117 (B2), n/a–n/a.

Gao, Y., Ye, H., Mao, J., Li, Y., 2013. Geology, geochemistry and genesis of the Qianfanling quartz-vein Mo deposit in Songxian County, Western Henan Province, China. Ore Geol. Rev. 55, 13–28.

Gautheron, C., Tassan-Got, L., Barbarand, J., Pagel, M., 2009. Effect of alpha-damage annealing on apatite (U-Th)/He thermochronology. Chem. Geol. 266 (3-4), 157–170.

Glorie, S., Alexandrov, I., Nixon, A., Jepson, G., Gillespie, J., Jahn, B.-M., 2017. Thermal and exhumation history of Sakhalin Island (Russia) constrained by apatite U-Pb and fission track thermochronology. J. Asian Earth Sci. 143, 326–342.

Glorie, S., Otasevic, A., Gillespie, J., Jepson, G., Danišík, M., Zhimulev, F.I., Gurevich, D., Zhang, Z., Song, D., Xiao, W., 2019. Thermo-tectonic history of the Junggar Alatau within the Central Asian Orogenic Belt (SE Kazakhstan, NW China): Insights from integrated apatite U/Pb, fission track and (U-Th)/He thermochronology. Geosci. Front. 10 (6), 2153–2166.

Gong, L., Kohn, B.P., Zhang, Z., Xiao, B., Wu, L., Chen, H., 2021. Exhumation and preservation of Paleozoic porphyry Cu deposits: Insights from the Yandong deposit, southern Central Asian orogenic belt. Econ. Geol. 116, 607–628.

Grimmer, J.C., Jonckheere, R., Enkelmann, E., Ratschbacher, L., Hacker, B.R., Blythe, A. E., Wagner, G.A., Wu, Q., Liu, S., Dong, S., 2002. Cretaceous-Cenozoic history of the southern Tan-Lu fault zone: apatite fission-track and structural constraints from the Dabie Shan (eastern China). Tectonophysics 359 (3-4), 225–253.

Guo, B.o., Yan, C., Zhang, S., Han, J., Yun, H., Tan, H., Song, Q., Meng, F., Tang, L., 2018. Geochemical and geological characteristics of the granitic batholith and Yuku concealed Mo-W deposit at the southern margin of the North China Craton. Geol. J. 55 (1), 95–116.

Huang, Y., Hu, R., Bi, X., Fu, S., Peng, K., Gao, W., Oyebamiji, A., Zhaanbaeva, A., 2019. Low-temperature thermochronology of the Carlin-type gold deposits in southwestern Guizhou, China: Implications for mineralization age and geological thermal events. Ore Geol. Rev. 115, 103178. https://doi.org/10.1016/j.oregeorev.2019.103178.

Jepson, G., Carrapa, B., George, S.W.M., Triantafyllou, A., Egan, S.M., Constenius, K.N., Gehrels, G.E., Ducea, M.N., 2021. Resolving mid-to upper-crustal exhumation through apatite petrochronology and thermochronology. Chem. Geol. 565, 120071. https://doi.org/10.1016/j.chemgeo.2021.120071.

Jepson, G., Glorie, S., Konopelko, D., Gillespie, J., Danišík, M., Mirkamalov, R., Mamadjanov, Y., Collins, A.S., 2018. Low-temperature thermochronology of the Chatkal-Kurama terrane (Uzbekistan-Tajikistan): Insights into the Meso-Cenozoic thermal history of the western Tian Shan. Tectonics 37 (10), 3954–3969.

Jin, C., Liu, Q., Liang, W., Roberts, A.P., Sun, J., Hu, P., Zhao, X., Su, Y., Jiang, Z., Liu, Z., Duan, Z., Yang, H., Yuan, S., 2018. Magnetostratigraphy of the Fenghuoshan Group in the Hoh Xil Basin and its tectonic implications for India-Eurasia collision and Tibetan Plateau deformation. Earth Planet. Sci. Lett. 486, 41–53.

Ketcham, R.A., Carter, A., Donelick, R.A., Barbarand, J., Hurford, A.J., 2007. Improved modeling of fission-track annealing in apatite. Am. Mineral. 92 (5-6), 799–810.

Ketcham, R.A., Donelick, R.A., Carlson, W.D., 1999. Variability of apatite fission-track annealing kinetics: III. Extrapolation to geological time scales. Am. Mineral. 84 (9), 1235–1255.

Kirkland, C.L., Yakymchuk, C., Szilas, K., Evans, N., Hollis, J., McDonald, B., Gardiner, N. J., 2018. Apatite: a U-Pb thermochronometer or geochronometer? Lithos 318-319, 143–157.

Klemm, L.M., Pettke, T., Heinrich, C.A., 2008. Fluid and source magma evolution of the Questa porphyry Mo deposit, New Mexico, USA. Miner. Deposita 43 (5), 533–552.

Larsson, D., Söderlund, U., 2005. Lu-Hf apatite geochronology of mafic cumulates: an example from a Fe-Ti mineralization at Smålands Taberg, southern Sweden. Chem. Geol. 224 (4), 201–211.

Laslett, G.M., Kendall, W.S., Gleadow, A.J.W., Duddy, I.R., 1982. Bias in measurement of fission-track length distributions. Nucl. Tracks Radiat. Meas. 6 (2-3), 79–85.

Leng, C.B., Cooke, D.R., Hou, Z.Q., Evans, N.J., Zhang, X.C., Chen, W.T., Danišík, M., McInnes, B., Yang, J.H., 2018. Quantifying exhumation at the giant Pulang porphyry Cu-Au deposit using U-Pb-He dating. Econ. Geol. 113, 1077–1092.

Li, D., Han, J., Zhang, S., Yan, C., Cao, H., Song, Y., 2015. Temporal evolution of granitic magmas in the Luanchuan metallogenic belt, east Qinling Orogen, central China: Implications for Mo metallogenesis. J. Asian Earth Sci. 111, 663–680.

Li, N., Chen, Y.-J., Pirajno, F., Gong, H.-J., Mao, S.-D., Ni, Z.-Y., 2012a. LA-ICP-MS zircon U-Pb dating, trace element and Hf isotope geochemistry of the Heyu granite batholith, eastern Qinling, central China: implications for Mesozoic tectono-magmatic evolution. Lithos 142-143, 34–47.

Li, N., Ulrich, T., Chen, Y.J., Thomsen, T.B., Pease, V., Pirajno, F., 2012b. Fluid evolution of the Yuchiling porphyry Mo deposit, East Qinling, China. Ore Geol. Rev. 48, 442–459.

Li, N., Chen, Y.-J., Pirajno, F., Ni, Z.-Y., 2013. Timing of the Yuchiling giant porphyry Mo system, and implications for ore genesis. Miner. Deposita 48 (4), 505–524.

Li, N., Chen, Y.-J., Santosh, M., Pirajno, F., 2018. Late Mesozoic granitoids in the Qinling Orogen, Central China, and tectonic significance. Earth Sci. Rev. 182, 141–173.

Li, N., Derrey, I.T., Holtz, F., Horn, I., Weyer, S., Xi, W., 2021. Molybdenum solubility and partitioning in H_2O-CO_2-NaCl fluids at 600° C and 200 MPa. Chem. Geol. 583, 120438.

Li, N., Pirajno, F., 2017. Early Mesozoic Mo mineralization in the Qinling Orogen: an overview. Ore Geol. Rev. 81, 431–450.

Li, X., Yang, X., Xia, B., Gong, G., Shan, Y., Zeng, Q., Li, W., Sun, W., 2011. Exhumation of the Dahinggan Mountains, NE China from the Late Mesozoic to the Cenozoic: New evidence from fission-track thermochronology. J. Asian Earth Sci. 42 (1-2), 123–133.

Li, Y., Zhang, D., Sun, X., Lv, C., 2019. Application of apatite fission-track analysis and zircon U-Pb geochronology to study the hydrothermal ore deposits in the Lesser Hinggan Range: Exhumation history and implications for mineral exploration. J. Geochem. Explor. 199, 141–164.

Liu, Q., Li, H., Shao, Y., Bala Girei, M., Jiang, W., Yuan, H., Zhang, X.u., 2021. Age, genesis, and tectonic setting of the Qiushuwan Cu-Mo deposit in East Qinling

(Central China): constraints from Sr-Nd-Hf isotopes, zircon U-Pb and molybdenite Re-Os dating. Ore Geol. Rev. 132, 103998. https://doi.org/10.1016/j.oregeorev.2021.103998.
Mao, J., Du, A., Seltmann, R., Yu, J., 2003. Re-Os ages for the Shameika porphyry Mo deposit and the Lipovy Log rare metal pegmatite, central Urals, Russia. Miner. Deposita 38 (2), 251–257.
Mao, J.W., Pirajno, F., Xiang, J.F., Gao, J.J., Ye, H.S., Li, Y.F., Guo, B.J., 2011. Mesozoic molybdenum deposits in the east Qinling-Dabie orogenic belt: characteristics and tectonic settings. Ore Geol. Rev. 43 (1), 264–293.
Mao, J.W., Xie, G.Q., Bierlein, F., Qü, W.J., Du, A.D., Ye, H.S., Pirajno, F., Li, H.M., Guo, B.J., Li, Y.F., Yang, Z.Q., 2008. Tectonic implications from Re-Os dating of Mesozoic molybdenum deposits in the East Qinling-Dabie orogenic belt. Geochim. Cosmochim. Acta 72 (18), 4607–4626.
Mao, J., Ye, H.S., Wang, R.T., Dai, J.Z., Jian, W., Xiang, J.F., Zhou, K., Meng, F., 2009. Mineral deposit model of Mesozoic porphyry Mo and vein-type Pb-Zn-Ag ore deposits in the eastern Qinling, central China and its implication for prospecting. Geol. Bull. China 28, 72–79 (in Chinese with English abstract).
Maruyama, S., Isozaki, Y., Kimura, G., Terabayashi, M., 1997. Paleogeographic maps of the Japanese Islands: Plate tectonic synthesis from 750 Ma to the present. Isl. Arc 6 (1), 121–142.
Márton, I., Moritz, R., Spikings, R., 2010. Application of low-temperature thermochronology to hydrothermal ore deposits: Formation, preservation and exhumation of epithermal gold systems from the Eastern Rhodopes, Bulgaria. Tectonophysics 483 (3-4), 240–254.
McDowell, F.W., McIntosh, W.C., Farley, K.A., 2005. A precise ^{40}Ar-^{39}Ar reference age for the Durango apatite (U–Th)/He and fission-track dating standard. Chem. Geol. 214 (3-4), 249–263.
McInnes, B.I., Farley, K.A., Sillitoe, R.H., Kohn, B.P., 1999. Application of apatite (U-Th)/He thermochronometry to the determination of the sense and amount of vertical fault displacement at the Chuquicamata porphyry copper deposit, Chile. Econ. Geol. 94, 937–947.
McInnes, B.I., Evans, N.J., Fu, F.Q., Garwin, S., 2005. Application of thermochronology to hydrothermal ore deposits. Rev. Mineral. Geochem. 58, 467–498.
Meng, Q.-R., Zhang, G.-W., 2000. Geologic framework and tectonic evolution of the Qinling orogen, central China. Tectonophysics 323 (3-4), 183–196.
Paton, C., Hellstrom, J., Paul, B., Woodhead, J., Hergt, J., 2011. Iolite: Freeware for the visualisation and processing of mass spectrometric data. J. Anal. At. Spectrom. 26 (12), 2508. https://doi.org/10.1039/c1ja10172b.
Patriat, P., Achache, J., 1984. India-Eurasia collision chronology has implications for crustal shortening and driving mechanism of plates. Nature 311 (5987), 615–621.
Qian, Z., Yang, F., Liu, C., Xue, F., Santosh, M., Yang, B., Zhang, S., Kim, S.W., 2021. Late Mesozoic Huangbeiling S-type granite in the East Qinling Orogen, China: Geochronology, petrogenesis and implications for tectonic evolution. Geochemistry. https://doi.org/10.1016/j.chemer.2021.125857.
Reiners, P.W., 2005. Zircon (U-Th)/He thermochronometry. Rev. Mineral. Geochem. 58 (1), 151–179.
Reiners, P.W., Nicolescu, S., 2006. Measurement of parent nuclides for (U-Th)/He chronometry by solution sector ICP-MS. ARHDL Report 1, 1–33.
Schoene, B., Bowring, S.A., 2006. U-Pb systematics of the McClure Mountain syenite: thermochronological constraints on the age of the ^{40}Ar/^{39}Ar standard MMhb. Contrib. Miner. Petrol. 151 (5), 615–630.
Stockli, D.F., Farley, K.A., Dumitru, T.A., 2000. Calibration of the apatite (U-Th)/He thermochronometer on an exhumed fault block, White Mountains, California. Geology 28, 983–986.
Sun, X., Leng, C.-B., Hollings, P., Song, Q.-J., Li, R.-Y., Wan, X.-Q., 2021. New ^{40}Ar/^{39}Ar and (U-Th)/He dating for the Zhunuo porphyry Cu deposit, Gangdese belt, southern Tibet: implications for pulsed magmatic-hydrothermal processes and ore exhumation and preservation. Miner. Deposita 56 (5), 917–934.
Tang, L.i., Wagner, T., Fusswinkel, T., Zhang, S.-T., Xu, B.o., Jia, L.-H., Hu, X.-K., 2021a. Magmatic-hydrothermal evolution of an unusual Mo-rich carbonatite: a case study using LA-ICP-MS fluid inclusion microanalysis and He-Ar isotopes from the Huangshui'an deposit, Qinling, China. Miner. Depos. 56 (6), 1133–1150.
Tang, L.i., Zhao, Y.u., Zhang, S.-T., Sun, L.i., Hu, X.-K., Sheng, Y.-M., Zeng, T., 2021b. Origin and evolution of a porphyry-breccia system: Evidence from zircon U-Pb, molybdenite Re-Os geochronology, in situ sulfur isotope and trace elements of the Qiyugou deposit, China. Gondwana Res. 89, 88–104.
Tapponnier, P., Molnar, P., 1977. Active faulting and tectonics in China. J. Geophys. Res. 82 (20), 2905–2930.
The Second Geological Exploration Institute of the Bureau of Geology and Mineral Exploration and Development of Henan Province (TSGEI), 2009. Mineral survey report of Yumugou Mo-W deposit in the Luanchuan County, Henan Province, pp. 1-66 (in Chinese).
Thiede, R.C., Sobel, E.R., Chen, J., Schoenbohm, L.M., Stockli, D.F., Sudo, M., Strecker, M.R., 2013. Late Cenozoic extension and crustal doming in the India-Eurasia collision zone: New thermochronologic constraints from the NE Chinese Pamir. Tectonics 32 (3), 763–779.
Thomson, S.N., Gehrels, G.E., Ruiz, J., Buchwaldt, R., 2012. Routine low-damage apatite U-Pb dating using laser ablation-multicollector-ICPMS. Geochem. Geophys. Geosyst. 13 (2), n/a–n/a.
Vermeesch, P., 2009. RadialPlotter: A Java application for fission track, luminescence and other radial plots. Radiat. Meas. 44 (4), 409–410.
Vermeesch, P., 2018. IsoplotR: A free and open toolbox for geochronology. Geosci. Front. 9 (5), 1479–1493.
Wang, C., Deng, J., Bagas, L., Wang, Q., 2017. Zircon Hf–isotopic mapping for understanding crustal architecture and metallogenesis in the Eastern Qinling Orogen. Gondwana Res. 50, 293–310.
Wang, C., Rao, S., Shi, K., Bagas, L., Chen, Q.i., Zhu, J., Duan, H., Liu, L., 2021a. Rutile in Amphibolite Facies Metamorphic Rocks: A Rare Example from the East Qinling Orogen, China. Appl. Sci. 11 (18), 8756. https://doi.org/10.3390/app11188756.
Wang, C., Deng, J., Bagas, L., He, X., Zhang, J., 2021b. Origin and classification of the Late Triassic Huaishuping gold deposit in the eastern part of the Qinling-Dabie Orogen, China: implications for gold metallogeny. Miner. Deposita 56 (4), 725–742.
Wang, G., Li, S., Wu, Z., Suo, Y., Guo, L., Wang, P., Liu, Y., 2019a. Early Paleogene strike-slip transition of the Tan-Lu Fault Zone across the southeast Bohai Bay Basin: Constraints from fault characteristics in its adjacent basins. Geol. J. 54 (2), 835–849.
Wang, J., Zhai, Y., Liu, J., Liu, Z., Liu, J., 2008. A new approach to post-ore change and preservation of ore deposits: Fission track analysis. Advances in Earth Science 23, 421–427 (in Chinese with English abstract).
Wang, S., Li, B., Zhang, X., Wang, P., Chao, W., Ye, H., Yang, Y., 2019b. Genesis of the Huoshenmiao Mo deposit in the Luanchuan ore district, China: Constraints from geochronology, fluid inclusion, and H-O-S isotopes. Geosci. Front. 10 (1), 331–349.
Wang, Y.H., Zhang, F.F., Liu, J.J., Xue, C.J., Li, B.C., Xian, X.C., 2018. Ore genesis and hydrothermal evolution of the Donggebi porphyry Mo deposit, Xinjiang, northwest China: Evidence from isotopes (C, H, O, S, Pb), fluid inclusions, and molybdenite Re-Os dating. Econ. Geol. 113, 463–488.
Wolf, R.A., Farley, K.A., Kass, D.M., 1998. Modeling of the temperature sensitivity of the apatite (U-Th)/He thermochronometer. Chem. Geol. 148 (1-2), 105–114.
Wu, Y.-S., Chen, Y.-J., Zhou, K.-F., 2017. Mo deposits in Northwest China: Geology, geochemistry, geochronology and tectonic setting. Ore Geol. Rev. 81, 641–671.
Wu, Z.L., Zhang, S.T., Xu, T., Cao, H.W., Pei, Q.M., Deng, M.Z., Tang, C.H., Zhang, P., 2015. Compositional characteristics, petrogenesis and metallogenic significance of biotite from granite in the Huangbeiling-Zhongyuku region of Luanchuan ore concentration area. J. Mineral. Petrol. 35, 11–19 (in Chinese with English abstract).
Xu, J., Zhu, G., 1994. Tectonic models of the Tan-Lu fault zone, eastern China. Int. Geol. Rev. 36 (8), 771–784.
Xue, F., Wang, G., Santosh, M., Yang, F., Shen, Z., Kong, L., Guo, N., Zhang, X., Jia, W., 2018. Geochemistry and geochronology of ore-bearing and barren intrusions in the Luanchuan ore fields of East Qinling metallogenic belt, China: diverse tectonic evolution and implications for mineral exploration. J. Asian Earth Sci. 157, 57–77.
Xue, L., Wang, G., Tang, L.i., Cao, Y.i., Du, J., Du, Y., Luo, L., Cheng, H., 2021a. Genesis and hydrothermal evolution of the Zhazigou skarn W (Mo) deposit, East Qinling, China: Constraints from fluid inclusions and H-O-S-Pb isotopes. Ore Geol. Rev. 138, 104374. https://doi.org/10.1016/j.oregeorev.2021.104374.
Xue, L., Wang, G., Du, Y., Cao, Y., 2021b. Genesis and fluid evolution of the Yuku porphyry Mo deposit, East Qinling orogen, China. Geol. J.. https://doi.org/10.1002/gj.4191.
Yang, F., Santosh, M., Glorie, S., Xue, F., Zhang, S., Zhang, X., 2020a. Apatite geochronology and chemistry of Luanchuan granitoids in the East Qinling Orogen, China: Implications for petrogenesis, metallogenesis and exploration. Lithos 378-379, 105797. https://doi.org/10.1016/j.lithos.2020.105797.
Yang, F., Santosh, M., Glorie, S., Jepson, G., Xue, F., Kim, S.W., 2020b. Meso-Cenozoic multiple exhumation in the Shandong Peninsula, eastern North China Craton: Implications for lithospheric destruction. Lithos 370-371, 105597. https://doi.org/10.1016/j.lithos.2020.105597.
Yang, F., Wang, G., Cao, H., Li, R., Tang, L., Huang, Y., Zhang, H., Xue, F., Jia, W., Guo, N., 2017a. Timing of formation of the Hongdonggou Pb-Zn-Ag polymetallic ore deposit, Henan Province, China: Evidence from Rb-Sr isotopic dating of sphalerites. Geosci. Front. 8, 605–616.
Yang, F., Wang, G., Santosh, M., Li, R., Tang, L.i., Cao, H., Guo, N., Liu, C., 2017b. Delineation of potential exploration targets based on 3D geological modeling: A case study from the Laoangou Pb-Zn-Ag polymetallic ore deposit, China. Ore Geol. Rev. 89, 228–252.
Yang, F., Xue, F., Santosh, M., Wang, G., Kim, S.W., Shen, Z., Jia, W., Zhang, X., 2019. Late Mesozoic magmatism in the East Qinling Orogen, China and its tectonic implications. Geosci. Front. 10 (5), 1803–1821.
Yang, Y., Li, N., Yang, Y., 2009. Fluid inclusion study of the Nannihu porphyry Mo-W deposit, Luanchuan county, Henan Province. Acta Petrologica Sinica 25, 2550–2562 (in Chinese with English abstract).
Yang, Y.-F., Li, N., Chen, Y.-J., 2012. Fluid inclusion study of the Nannihu giant porphyry Mo-W deposit, Henan Province, China: implications for the nature of porphyry ore-fluid systems formed in a continental collision setting. Ore Geol. Rev. 46, 83–94.
Yang, Y., Chen, Y.-J., Zhang, J., Zhang, C., 2013. Ore geology, fluid inclusions and four-stage hydrothermal mineralization of the Shangfanggou giant Mo-Fe deposit in Eastern Qinling, central China. Ore Geol. Rev. 55, 146–161.
Yang, Y.-F., Chen, Y.-J., Pirajno, F., Li, N., 2015. Evolution of ore fluids in the Donggou giant porphyry Mo system, East Qinling, China, a new type of porphyry Mo deposit: evidence from fluid inclusion and H-O isotope systematics. Ore Geol. Rev. 65, 148–164.
Yuan, W., 2016. Thermochronological method of revealing conservation and changes of mineral deposits. Acta Petrologica Sinica 32, 2571–2578 (in Chinese with English abstract).
Zeitler, P.K., Herczeg, A.L., McDougall, I., Honda, M., 1987. U-Th-He dating of apatite: A potential thermochronometer. Geochim. Cosmochim. Acta 51 (10), 2865–2868.
Zhang, R., Zhang, D., Wu, M., Hou, H., Li, X., 2021a. Genesis of the Shiyaogou Porphyry Mo Deposit at East Qinling, China: evidence from geochronological, fluid inclusion, geochemical whole-rock and isotope studies. Ore Geol. Rev. 136, 104263. https://doi.org/10.1016/j.oregeorev.2021.104263.
Zhang, X.-F., Li, W.-C., Wang, R., Zhang, L., Qiu, K.-F., Wang, Y.-Q., 2021b. Preservation of Xiuwacu W-Mo deposit and its constraint on the uplifting history of Eastern Tibetan Plateau. Ore Geol. Rev. 132, 103995. https://doi.org/10.1016/j.oregeorev.2021.103995.

Zhang, Y., Cao, H., Xu, M.o., Zhang, S., Tang, L.i., Wang, S., Pei, Q., Cai, G., Shen, T., 2018. Petrogenesis of the late Mesozoic highly fractionated I-type granites in the Luanchuan district: implications for the tectono-magmatic evolution of eastern Qinling. Geosci. J. 22 (2), 253–272.

Zhang, Y., Zhang, S., Xu, M.o., Jiang, X., Li, J., Wang, S., Li, D., Cao, H., Zou, H., Fang, Y. i., 2015. Geochronology, geochemistry, and Hf isotopes of the Jiudinggou molybdenum deposit, Central China, and their geological significance. Geochem. J. 49 (4), 321–342.

Zhao, J., Qin, K., Xiao, B.o., McInnes, B., Li, G., Evans, N., Cao, M., Li, J., 2016. Thermal history of the giant Qulong Cu-Mo deposit, Gangdese metallogenic belt, Tibet: constraints on magmatic-hydrothermal evolution and exhumation. Gondwana Res. 36, 390–409.

Zhao, Z.C., 2018. Petrogenesis and Mineralization Potential of the Huangbeiling Granite Pluton in Luanchuan, Henan Province. China Univ. Geosci. (Beijing) 24–48 (in Chinese with English abstract).

Zhou, T., Zeng, Q., Gao, S., Chu, S., Yang, J., 2020. Geochronology, geochemistry and fluid inclusions of the Yechangping giant porphyry-skarn Mo-W deposit, East Qinling, China. Ore Geol. Rev. 127, 103823. https://doi.org/10.1016/j.oregeorev.2020.103823.

Zhu, L., Zhang, G., Guo, B.o., Lee, B., Gong, H., Wang, F., 2010. Geochemistry of the Jinduicheng Mo-bearing porphyry and deposit, and its implications for the geodynamic setting in East Qinling, PR China. Geochemistry 70 (2), 159–174.